PHILOSOPHICAL TRANSACTIONS A

royalsocietypublishing.org/journal/rsta

Review

Cite this article: Georgoulis MK, Nindos A, Zhang H. 2019 The source and engine of coronal mass ejections. *Phil. Trans. R. Soc. A* **377**: 20180094.
http://dx.doi.org/10.1098/rsta.2018.0094

Accepted: 6 March 2019

One contribution of 9 to a theme issue 'Solar eruptions and their space weather impact'.

Subject Areas:
astrophysics, plasma physics, computational physics, computer modelling and simulation, mathematical physics

Keywords:
solar eruptions, coronal mass ejections, interpretation

Author for correspondence:
Manolis K. Georgoulis
e-mail: manolis.georgoulis@phy-astr.gsu.edu

The source and engine of coronal mass ejections

Manolis K. Georgoulis[1,2], Alexander Nindos[3] and Hongqi Zhang[4]

[1]Department of Physics and Astronomy, Georgia State University, Atlanta 30303 GA, USA
[2]RCAAM of the Academy of Athens, Athens 11527, Greece
[3]Department of Physics, University of Ioannina, Ioannina 45110, Greece
[4]National Astronomical Observatories, Chinese Academy of Sciences, Beijing 100101, People's Republic of China

MKG, 0000-0001-6913-1330

Coronal mass ejections (CMEs) are large-scale expulsions of coronal plasma and magnetic field propagating through the heliosphere. Because CMEs are observed by white-light coronagraphs which, by design, occult the solar disc, supporting disc observations (e.g. in EUV, soft X-rays, Halpha and radio) must be employed for the study of their source regions and early development phases. We review the key properties of CME sources and highlight a certain causal sequence of effects that may occur whenever a strong (flux-massive and sheared) magnetic polarity inversion line develops in the coronal base of eruptive active regions (ARs). Storing non-potential magnetic energy and helicity in a much more efficient way than ARs lacking strong polarity inversion lines, eruptive regions engage in an irreversible course, making eruptions inevitable and triggered when certain thresholds of free energy and helicity are crossed. This evolution favours the formation of pre-eruption magnetic flux ropes. We describe the steps of this plausible path to sketch a picture of the pre-eruptive phase of CMEs that may apply to most events, particularly the ones populating the high end of the energy/helicity distribution, that also tend to have the strongest space-weather implications.

This article is part of the theme issue 'Solar eruptions and their space weather impact'.

THE ROYAL SOCIETY PUBLISHING

1. Introduction

The solar atmosphere exhibits a wealth of dynamic phenomena. The most powerful of them are coronal mass ejections (CMEs) and flares. CMEs are large-scale expulsions (10^{14}–10^{16}) gr of magnetized coronal plasma into the heliosphere. Their speeds range from about 100 km s^{-1} to more than 3000 km s^{-1}, with an average of approximately 500 km s^{-1} [1]. CMEs beyond the solar disc are detected in white-light coronagraphs (see figure 1, for an example) due to Thomson scattering of the photospheric light by the electrons of the ejected plasma. Flares result in the impulsive release of energy in the solar atmosphere, with major events occurring exclusively in active regions (ARs). Plasma is heated and particles are accelerated to relativistic energies on short timescales. A large flare may require the acceleration of 10^{35} electrons s^{-1} to energies higher than 20 keV for timescales of tens of seconds (e.g. [2]).

Solar flares and CMEs have an impact on geospace that can range from benign to severe. This issue includes several comprehensive reviews (e.g. Daglis *et al.*, Balasis *et al.* and Vourlidas *et al.*) detailing this impact. This said, CME consequences are more persistent. In case an interplanetary CME transiting through Earth has a strong, persistent, terrestrially southward magnetic field component, it can resonate with Earth's radiation belts via electrostatic waves and/or magnetically reconnect with Earth's magnetosphere, either way channelling its trapped solar particles to Earth's upper atmosphere. Magnetic reconnection also leads to greatly enhanced geomagnetic fields in a situation known as a geomagnetic storm. It is often deemed important to physically understand the origin of CMEs to be able to forecast their consequences.

The occurrence rates of both CMEs and flares vary within the solar cycle. For example, on average one CME is produced per day at solar minimum and five per day at solar maximum (e.g. [1]). Averaged over a solar cycle, the occurrence rate of CMEs is about 2–3 per day; this rate is smaller than that of flares (about 5–6 per day, counting also events smaller than GOES C-class), which indicates that CMEs and flares do not necessarily correlate one-to-one. When they do, the flare is called *eruptive*, otherwise it is called *confined*. The flare-CME association likelihood increases with flare magnitude; the largest (i.e. of GOES class X2–X3 and above) flares are one-to-one associated with CMEs [3,4].

Since CMEs are observed by coronagraphs which, by design, occult the solar disc, their initiation and early stages can be studied only from observations obtained by other instruments such as EUV and soft X-ray (SXR) images, Hα filtergrams and radio interferometers. These studies (e.g. see [5–7] for reviews) have revealed that CMEs originate from structures with a variety of spatial scales that range from X-ray bright points as small as tens of thousands of km across (see [8]) to polar crown filaments as large as hundreds of thousands of km long. Fast CMEs, which are the most important in terms of space weather ramifications, typically originate from ARs and are associated with both flares and eruptive filaments[1] which delineate the AR's magnetic polarity inversion line (PIL; e.g. [9,10]). Quiet-Sun CMEs are usually slower than the ones launched from ARs. They typically originate from extended quiet-Sun filaments or polar crowns (e.g. [11,12]).

The combination of off-limb white-light observations with disc observations has shed much-needed light on the low-atmosphere counterparts of the various CME structures, as observed by coronagraphs. CMEs and other coronal ejections come in many shapes, but much of the observed variety is due to projection effects. Spacecraft-directed CMEs often appear to surround the occulting disc of the coronagraph and are thus known as halo CMEs. One of the simplest forms (usually referred to as 'typical') is the three-part-structure CME comprising a leading edge, followed by a dark void (cavity) and a bright core (see figure 1, for a typical example). The leading edge is compressed CME-overlying material piled together during the initial expansion phase. The void is assumed to stem from the prominence cavity as a magnetic flux rope seen edge-on. With the term 'flux rope', we mean a twisted flux tube whose field lines wind about a common, relatively untwisted, axis field line in the interior of the tube. This interpretation is supported by

[1]Filaments, also known as prominences when observed above the limb, are lanes of cool plasma magnetically threaded in the upper chromosphere and low corona.

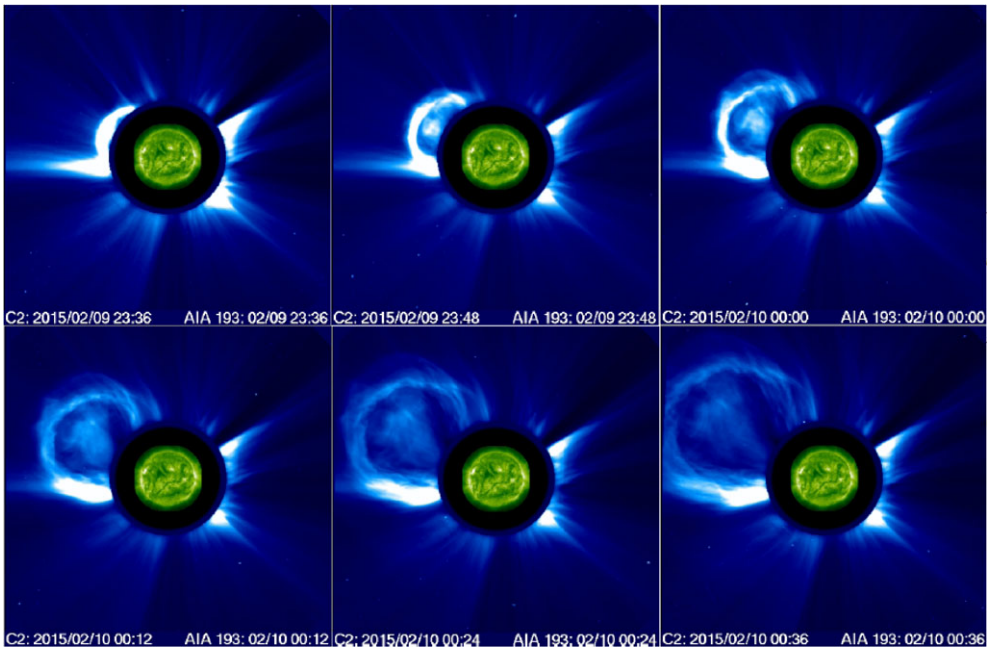

Figure 1. A 60-min evolution of a CME in the field of view of the SOHO/LASCO C2 coronagraph. In each panel, the LASCO data are combined with the temporally best-matched SDO/AIA 193 Å data. The CME appears in the top-left quadrant in each image.

the fact that the tops of several cavities are rounded (figure 1). Vourlidas *et al.* [13] have found that at least 40% of CMEs have flux rope structures. The bright core corresponds to the erupting prominence.

CMEs are purely magnetic phenomena: in the strongly magnetized coronal plasma, where the plasma β parameter (i.e. the ratio of thermal to magnetic pressures) is much smaller than one, magnetic field lines act as material lines with plasma 'frozen in' along them. Observationally, CMEs are structures evidently organized by magnetic fields with spatial scales of the order of the solar radius ($R_\odot$) near the Sun, maintaining their apparent structural integrity over at least several solar radii.

CMEs are preceded by a relatively long phase (of the order few days to weeks) in which the magnetic field is gradually stressed and free (i.e. non-potential, due to electric currents) magnetic energy and magnetic helicity build up in local, AR or quiet-Sun filament, scales. The terms and notions of both magnetic free energy and magnetic helicity are discussed in §3. In most models (e.g. [14] and references therein), the pre-eruptive magnetic configuration features either a magnetic flux rope or a sheared magnetic arcade. These models argue that CMEs may result from a catastrophic loss of equilibrium between the magnetic forces acting on a structure possessing large amounts of free magnetic energy. These forces are the magnetic pressure and tension. The former is enhanced in structures of strong magnetic field which tend to expand into regions of weak magnetic field, while the latter is a restraining force keeping the magnetic structure contained and/or strapped by the overlying coronal field. Magnetic confinement fails, and a CME is produced, either resistively, due to magnetic reconnection, or due to some ideal instability that develops when the energy trapped in the stressed structure suffices to drive an outward expansion against the overlying large-scale coronal field [15]. An effect then observed—albeit rarely—in the post-eruption structure is an implosion (i.e. contraction) of the coronal loops to a new stable configuration, following the decrease of magnetic pressure caused by the eruptive coronal discharge [16,17].

The purpose of this review is to discuss the fundamental physical phenomena taking place until the CME initiation, along with the open questions that loom over some of these phenomena. For example, what, if any, sequence of physical processes makes an eruption inevitable? What is the configuration of the pre-eruption magnetic field? In addition to free magnetic energy, what is the role of magnetic helicity build-up in the initiation process? What mechanisms could act as CME triggers and drivers? Given their space weather importance, we focus on CMEs originating from ARs. In §2, we discuss the fundamental properties of ARs that produce CMEs and in §3 we define the relevant, fundamental physical quantities. A potential course toward CMEs, proposed here for the first time in its entirety, is outlined in §4, while mechanisms related to CME triggering and driving are discussed in §5. We summarize and conclude this review in §6.

2. Fundamental properties of source active regions

(a) Photospheric properties

There is a vast amount of literature on the properties of solar ARs that produce CMEs (e.g. see the review by Howard [18] and references therein). Up until relatively recently, it was common sense that the line-of-sight (normal, close to disc centre) component of the photospheric magnetic field remained virtually unchanged during solar eruptions (e.g. [19]). However, as was more recently shown, even the photosphere shows some unambiguously eruption-related changes (e.g. [20,21]). Regardless, coronal disturbances originated by CMEs have little effect on the photosphere due to the substantial difference between photospheric and coronal mass densities. The relative insensitivity of the photospheric footpoints in the eruption, on characteristic timescales of tens of minutes, has been dubbed 'inertial line-tying' of the photospheric magnetic field. Note, however, that line-tying may not be always very efficient during major flares (e.g. [22,23]).

There is little doubt that CMEs are mainly powered by magnetic energy due to force-free electric currents, flowing along the coronal magnetic field lines (e.g. see [24,25]). This, however, should not underestimate the presence and potential role of cross-field currents that are responsible for Lorentz forces, at least in, and slightly above, the photosphere (see §4) and in filaments magnetically sustained in the corona. The build-up of electric currents, in general, stresses the magnetic field, at the same time storing free magnetic energy into the corona. Free magnetic energy is the only energy budget available for release, that is, conversion into other forms. Observations show that stresses develop gradually; their build-up may start days or even weeks prior to the eruption. This is a direct consequence of the small photospheric driving speeds which peak at around $1\,\mathrm{km\,s^{-1}}$ and are hence much smaller than the coronal Alfven speed. This key observation justifies the assumption made by most models (see §5) that, in spite of the photospheric or low-atmospheric Lorentz forces, the coronal magnetic evolution can be described by a sequence of quasi-static force-free equilibria.

A telltale signature of the gradual build-up of electric currents in eruptive ARs is the development of conspicuous, flux-massive, high-gradient magnetic PILs (e.g. see [26]), where the photospheric magnetic field becomes sheared and aligns to the PIL, contrary to a current-free field that is typically perpendicular to the PIL. An example is given in figure 2, where we present photospheric vector magnetograms of NOAA AR 11429 which hosted several major eruptive events, including three X-class flares. In this AR, the strong PIL and the shear along it had already formed before the AR's rotation to the earthward solar hemisphere.

To the best of our knowledge—and we consider this a key feature of AR magnetism—there has never been a strong PIL without shear, and also there is no paradigm of ARs with intense PILs that fade away without giving at least one major eruption. By 'strong' or 'intense' PILs, we mean sheared PIL configurations along which the intensity of the magnetic field becomes higher than the local equipartition value (see §3 for more details). Conversely, cases of ARs that produce multiple eruptive flares but do not contain extended, strong and sheared PILs are rare, and they seldom, if at all, host flares stronger than GOES X1-class. An intense magnetic flux emergence scenario could potentially account for these exceptions: a new magnetic flux emerges

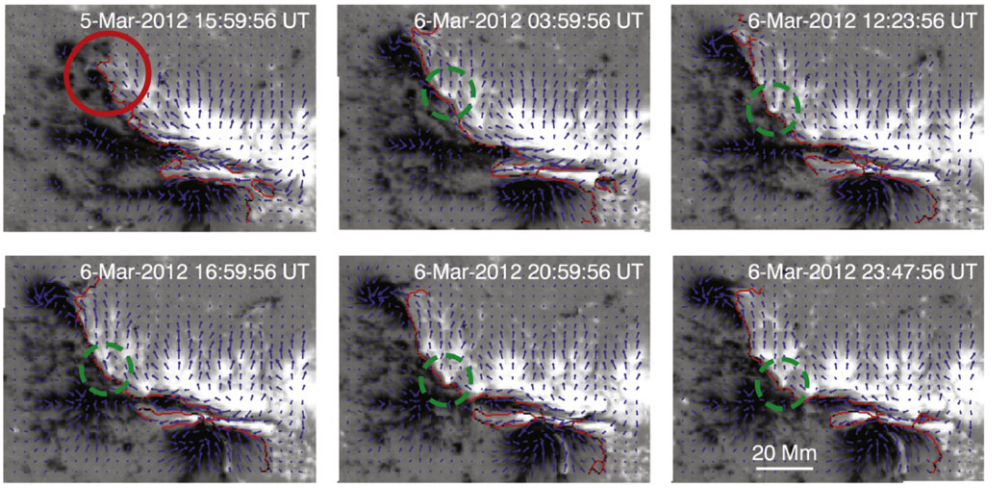

Figure 2. Evolution of the photospheric magnetic field prior to a twin major eruption. The grey-scale background and the arrows show the normal and horizontal components of the field, respectively. The red curve delineates the PIL, while the red circle and green dashed circles mark sites of flux emergence and shearing motions, respectively. Adapted from Chintzoglou *et al*. [27].

in the vicinity of a filament and an eruption occurs as a result of magnetic reconnection between the new and the pre-existing magnetic flux (e.g. [28–30]).

The low-coronal magnetic configuration above a photospheric PIL that can sustain a filament or prominence is called a filament channel. There is heated debate as to the physical mechanisms that could lead to the formation of filament channels, as well as about their topological properties (e.g. see the reviews by [7,14,31–33]). Observations show that the build-up of currents in AR filament channels may involve multiple processes: the first stage requires magnetic flux emergence. The newly emerged field may (e.g. [34,35]) or may not deviate much from the current-free (potential) state, but typically the amount of electric currents injected in the corona during the very first stages of flux emergence is small (e.g. [36,37]). In eruptive ARs, significant accumulation of currents starts as soon as the AR starts shaping its PIL (e.g. [36–39]). Electric currents along PILs are largely due to PIL-aligned shearing motions. While these peculiar AR motions are responsible for AR filament channels, the crucial agent in the formation of larger, quiet-Sun filaments is solar differential rotation. At a later stage, magnetic flux cancellation along the PIL could be observed: in this process, opposite magnetic polarities converge, collide and disappear (e.g. [40–42]). This process may also enhance complexity along the PILs, as discussed in §4 below. Note that flux emergence, shearing motions and flux cancellation may occur independently or in tandem in ARs that host major eruptive events.

(b) Coronal properties

Models of CME initiation (see §5) presume that the pre-eruptive coronal configuration is either a magnetic flux rope or a sheared magnetic arcade. In the latter case, the sheared arcade transitions to a flux rope during the eruption because there is no physical process that can produce a large-scale outward propagation without involving a flux rope. Motivated by this fact, a large number of works investigate the pre-eruptive coronal configurations using multi-wavelength observations. In principle, both sheared arcades and flux ropes can sustain dipped, sheared filament channels above PILs. However, deciphering the pre-eruptive coronal structure is difficult because routine magnetic field measurements above the photosphere are not available and because line-of-sight confusion is inevitable when imaging optically thin plasmas. This said, there are direct efforts that have aimed to constrain the properties of the coronal magnetic field by using

radio observations (e.g. see [43] for a review). Indirect ones often exploit the properties of filament barbs [44] or tornadoes [45].

Indirect evidence for the existence of flux ropes in eruptive ARs located close to the disc centre is provided by nonlinear force-free field (NLFFF) extrapolations of the photospheric magnetic field (e.g. [27,36,46–51]). The cadence of the available vector magnetograms is 12 min, at best,[2] providing an upper limit for the cadence of the NLFFF extrapolations. Therefore, such extrapolations—on top of being static approximations—cannot reproduce the rapidly changing fields that erupt at timescales well below 10 min. Moreover, using the photospheric boundary condition for extrapolations during major white-light flares can lead to widespread spurious results due to contamination. Most importantly, however, the onset of an eruption may well be associated with a non-negligible Lorentz force that renders the field non-force-free and the NLFFF extrapolations inadequate. In most cases, the inferred twist of the NLFFF, supposedly reconstructed flux ropes hardly exceeds one turn (see [53] and references therein), which makes it difficult to distinguish between them and sheared arcades. Finally, it has been reported that flux ropes and sheared arcades can coexist in the pre-eruptive configuration of some ARs (e.g. see [49]).

SXR and EUV observations of S-shaped or reverse S-shaped structures may also provide indirect evidence for the existence of pre-eruptive flux ropes. It has been established (e.g. [54]) that sigmoidal ARs are more likely to erupt, while Rust & Kumar [55] suggested that X-ray sigmoids represent the projections of helically kinked flux ropes along the line of sight, whose twist around their axis should be around one turn. However, Titov & Démoulin [56] proposed that sigmoids represent emission from a current layer in the separatrix formed by field lines that touch the PIL underneath the flux rope. In this light, Green *et al.* [57] pointed out that the association of sigmoidal structures with flux ropes is only valid if (i) they cross the PIL in the inverse direction of what potential field lines would do, and (ii) the sigmoidal structure survives an eruption, as only then the interpretation of the sigmoid in terms of a sheared arcade can be excluded [58]. However, the latter argument could be challenged in cases of major eruptions in which transient, eruption-related sigmoids erupt and disappear, leaving bright post-eruption arcades behind them.

In contrast to the formation of sheared arcades, naturally attributed to photospheric motions, sigmoidal structures, especially those associated with decaying, bipolar ARs, are usually formed via flux cancellation along the PIL (see [59]). An example, taken from Green *et al*. [57], is presented in figure 3. In these cases, both the photospheric and the coronal evolution are consistent with the model proposed by van Ballegooijen & Martens [40] in which a sheared arcade is transformed to a flux rope as a result of low-altitude magnetic reconnection. Such sigmoids may remain stable for several hours before eruption (e.g. [60]).

High-cadence, high-sensitivity EUV data obtained by the atmospheric imaging assembly (AIA) onboard the solar dynamics observatory (SDO) have revealed the existence of coherent 'hot channels' attributed to hot magnetic flux ropes. These structures appear sigmoidal when seen against the disc [61,62] and as round blobs or ring-like structures when seen above the limb (e.g. see [63] and references therein). An example presented in figure 4, taken from Patsourakos *et al*. [64], shows the formation of a hot, flux-rope-like structure triggered by a confined flare. Heating of these structures is achieved via magnetic reconnection: according to the standard model of eruptive flares (see §2c below) the reconnected magnetic flux underneath the CME is directed towards both the erupting flux rope and the flaring loops. Unlike erupting filaments, often showing fragmentation in Hα or the EUV, hot channels maintain their structural coherence throughout the eruption. The statistical study performed by Nindos *et al*. [63] showed that almost half of the eruptions associated with major limb flares involved hot, flux-rope-like structures.

In AIA observations, such structures appear from about 7 h [64] to a few minutes (e.g. [65,66]) prior to eruptions. Cases of formation during the eruption have also been reported (e.g. [67,68]), while older Yohkoh Soft X-ray Telescope (SXT) observations showed sigmoids persisting for much longer times without erupting. In most AIA observations, it has been demonstrated that the hot

[2]But notice the recent release of SDO/HMI higher-cadence vector magnetograms, discussed by Sun *et al*. [52].

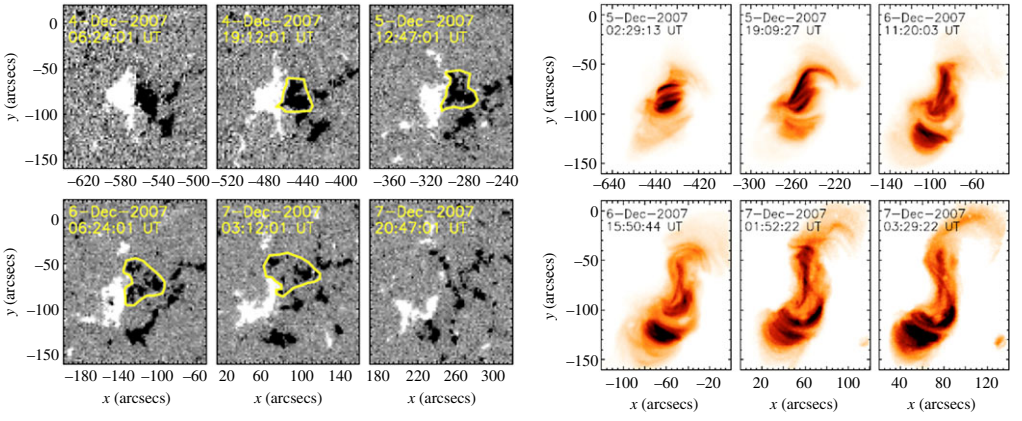

Figure 3. The three left-most columns show the evolution of the line-of-sight component of the magnetic field in a bipolar AR. The yellow contour encircles the area in which significant flux cancellation took place. The other columns show C-Poly filter SXR observations of the same AR. Reproduced with permission from Green *et al.* [57].

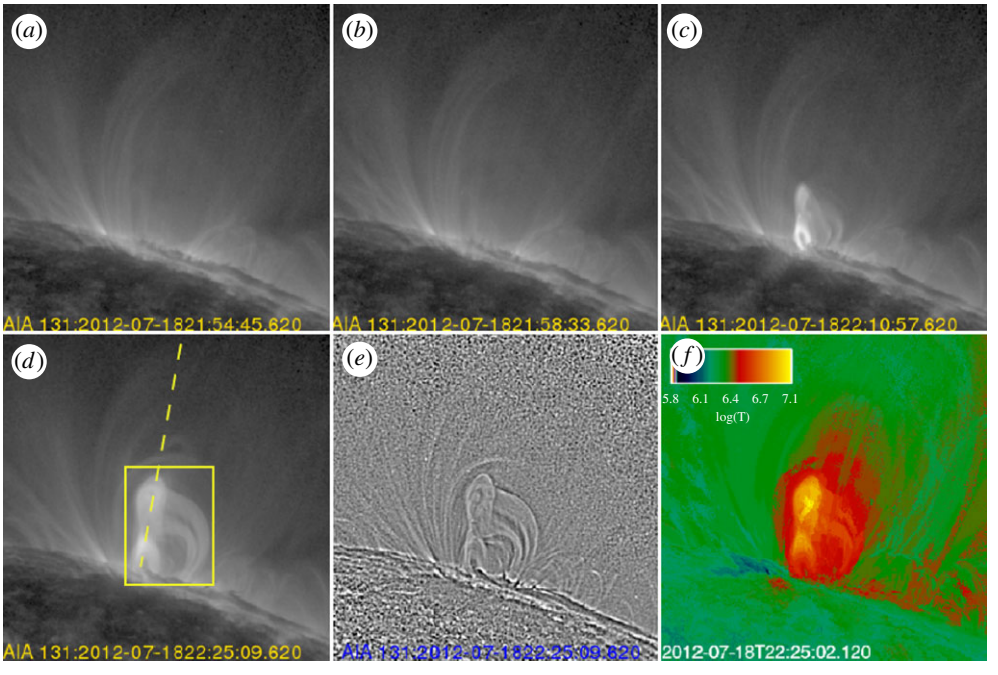

Figure 4. A confined flare observed in 131 Å. (*a*,*b*) The pre-event corona while (*c*,*d*) the development of the hot flux rope. (*e*,*f*) The image of (*d*) after wavelet enhancement and the corresponding temperature map, respectively. Adapted from Patsourakos *et al*. [64].

flux rope is formed by magnetic reconnection. In cases of on-the-fly, eruptive formation of flux ropes, reconnection could also be invoked for the interpretation of their heating: in the standard flare model, the reconnected magnetic flux underneath the CME is directed towards both the erupting flux rope and the flaring loops. In one exceptional case (see [62]) of a hot channel close to the disc centre, it was found that reconnection was triggered by a combination of flux emergence and sunspot rotation.

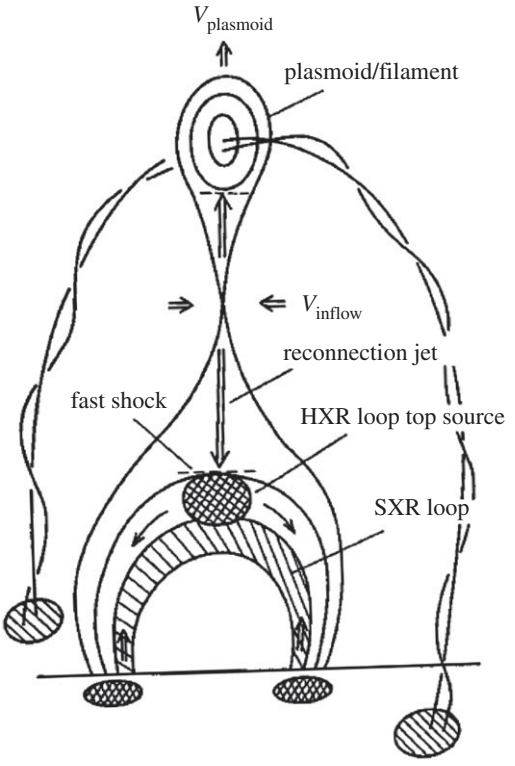

Figure 5. Sketch of the standard flare model as supported by Yohkoh observations. Adapted from Shibata *et al.* [76].

(c) Phenomenology of eruptive flares

Simultaneous near-Sun and solar-disc observations have shown that CMEs produced in ARs often exhibit a three-phase evolution (e.g. [69,70]). First, there is a slow-rise phase that may last from several minutes to a few hours, in which the filament darkens and slowly ascends, while coronal loops expand. This is followed by a rapid acceleration phase that occurs over timescales of a few minutes and corresponds to the progression of the eruption. Finally, there is a propagation phase in which the erupting structure interacts with the ambient solar wind and starts its transit into the heliosphere.

The acceleration phase is often described in terms of the so-called standard model of eruptive flares, which was developed in [71–74] and was refined in the 1990s by incorporating several observations achieved by the Yohkoh satellite (e.g. [75]). A very much simplified sketch of the standard flare model, used here only for visualization purposes, is shown in figure 5. Since its inception, it is being constantly improved, with a fully three-dimensional extension adding more realism to it developed by Aulanier and colleagues [77–80]. According to this model, the flux rope (indicated as 'plasmoid' in figure 5) that will eventually erupt is initially in a state of equilibrium, possibly due to the restraining action of the overlying field. Note that if there is no flux rope initially, magnetic reconnection will create one. As the eruption is triggered resistively by magnetic reconnection, or ideally, by a flux-rope instability, the flux rope starts rising, stretching its overlying field and forming an anti-parallel magnetic configuration in its wake. In this course, the downward and upward field lines below it approach each other and a current sheet is developed with magnetic reconnection eventually taking place there as well. This reconnection has two consequences: (i) it dissipates energy, giving rise to a flare below the reconnection region. The flare shows first at microwaves and hard X-rays, followed by a two-ribbon brightening in Hα and the EUV; and (ii) it cuts the 'restraining tethers' imposed by the overlying field and so

facilitates the rapid ascension of the flux rope, which gains additional poloidal magnetic flux. Due to the motion of the flux rope, the overlying closed field lines are pushed and piled up forming the CME's leading edge. Moreover, due to the external pressure, there is mass inflow into the current sheet that further drives reconnection and energy release in the form of emission, heating and particle acceleration.

The sequence of events suggested above has led several authors (e.g. [81]) to conclude that in erupting events CMEs and flares are different manifestations of the same physical process that ultimately converts free magnetic energy into kinetic (thermal and non-thermal) and radiative energies. This outlook has been strengthened by the temporal coincidence between the CME acceleration and flare impulsive phases, which is observed in several eruptive events (e.g. [69,82]).

In distinguishing eruptive and confined flares, we note that a full eruption might not be achieved, either due to an insufficient removal of the overlying field by the reconnection that takes place below the erupting structure [83], or due to a weakly decreasing magnetic field strength with height in the overlying corona, presenting a significant, restraining tension force [84].

3. Definition of fundamental physical quantities

By now, it has become clear that solar ARs are relatively isolated, singular, intensely magnetized configurations in the solar atmosphere. A fundamental quantity characterizing their evolution is their *magnetic flux*. The total (i.e. unsigned) magnetic flux Φ is the integrated magnetic intensity perpendicular to a given area, or boundary, S, of any geometry, planar or curved, namely,

$$\Phi = \int_S |\mathbf{B}\cdot\hat{\mathbf{n}}|\,\mathrm{d}S = \int_S |B_n|\,\mathrm{d}S, \tag{3.1}$$

where $\mathbf{B}$ is the magnetic field vector. Here, we have used the convention $\mathbf{B}\cdot\mathrm{d}\mathbf{S} = B_n\,\mathrm{d}S$ by means of the local, normal to S, unit vector $\hat{\mathbf{n}}$ ($\mathrm{d}\mathbf{S} = \mathrm{d}S\,\hat{\mathbf{n}}$) and the respective normal field component, $B_n = \mathbf{B}\,\hat{\mathbf{n}}$.

To comply with the prevailing paradigm in magnetohydrodynamics (MHD) (e.g. [85]), knowledge of the magnetic field $\mathbf{B}$ over a given area should be complemented by the velocity field vector $\mathbf{u}$ of the magnetized plasma in the boundary S. For typical solar AR applications, this boundary is the photosphere, where magnetic field measurements exist.

Magnetic flux Φ reflects the size of the AR studied: indeed, magnetic flux is an *extensive* quantity that does not provide information on the level or degree of complexity in the AR. Providing the flux of, say, a sunspot complex does not specify the complexity of the conglomeration (e.g. PILs or other features), but it simply says how flux-massive sunspots and surrounding plage are. The flux of NOAA AR 11429 (figure 2), for example, classifies it as a 'large' AR, but does not give any additional information. To gain knowledge into the complexity of the magnetic structures involved, one needs specific moments of the field $\mathbf{B}$ and its flux Φ that are *intensive* in nature, i.e. non-trivially related to the size of the structure. Key among them is the electric current density $\mathbf{J}$, provided by Ampére's Law:

$$\mathbf{J} = \frac{c}{4\pi}\nabla\times\mathbf{B}. \tag{3.2}$$

The above equation demonstrates that, provided sufficient spatial resolution, the current density $\mathbf{J}$ relates to the spatial gradients of the magnetic field: discontinuous or perturbed flux distributions give rise to more intense current densities. Current density essentially relates to a term of the magnetic energy, as well. The magnetic energy is simply the volume integral of the magnetic energy density $B^2/(8\pi)$, namely,

$$E_\mathrm{m} = \int_V \frac{B^2}{8\pi}\,\mathrm{d}V \tag{3.3}$$

in a volume V with lower (photospheric) boundary S. However, to accommodate a non-zero $\mathbf{J}$, the magnetic field should be different from a vacuum, minimum-energy curl-free configuration. Hence, as per Chandrasekhar [86,87], the magnetic field vector can always be decomposed

into a vacuum, curl-free, component $\mathbf{B_p}$ (also popularly known as 'potential' field) and a current-dependent, non-potential component $\mathbf{B_c}$, entirely responsible for $\mathbf{J}$. In an elaboration of equation (3.3), then, it can be shown [88] that by substituting $\mathbf{B_c} = \nabla \times \mathbf{A_c}$ by its generating vector potential $\mathbf{A_c}$, equation (3.3) can be written as

$$E_\mathrm{m} = \frac{1}{8\pi}\int_V B_p^2\,\mathrm{d}V + \frac{1}{2c}\int_V \mathbf{A_c}\cdot\mathbf{J}\,\mathrm{d}V, \tag{3.4}$$

where one also uses Ampére's Law, equation (3.2), for $\mathbf{B_c}$.

As expected, then, the current density impacts the magnetic energy E_m: next to an extensive term, relying entirely on the vacuum magnetic field $\mathbf{B_p}$ (the flux itself relies on it via equation (3.1) and $\mathbf{B_p}$ in V is entirely described by B_n in S (e.g. [89])), it adds an intensive term explicitly related to $\mathbf{J}$ and the vector potential for the non-potential field component. Again, large magnetic gradients, giving rise to large current densities in V, statistically enhance this energy term, popularly known as 'free', or non-potential, magnetic energy. It is the maximum amount of magnetic energy that can be released, resistively, i.e. via magnetic reconnection, or ideally, i.e. via expulsion of the current-carrying part of the structure, without any modification of B_n in the lower boundary S. The latter condition is a special case of a constant magnetic flux Φ on S that ignores changes in B_n due to velocity flows $\mathbf{u}$ on S. The release of the free magnetic energy is essentially a relaxation, theoretically able to return the magnetic structure to potentiality (e.g. [90]).

While this simple relaxation process could be the main theory underlying solar transients, such as flares, solid evidence proved it to be oversimplified (figure 5 and related discussion in §§2c). Indeed, the standard flare model made it clear that a plasmoidal part of the configuration is destabilized and ejected during the flare. This ejectum is practically the CME progenitor, also referred to as a flux rope in observational studies (§2). While this might be thought to return the structure to potentiality, it has become clear that, due to photospheric line-tying, the post-eruption structure continues to enclose non-zero electric current density (e.g. [25] and references therein). Therefore, the relaxation towards potentiality is all but imperfect.

In cases of confined flares (§§2c), there is energy released resistively due to magnetic reconnection in the corona, but there is also a topological invariant of the magnetic structure for the coronal magnetic field of the AR. This is the magnetic helicity H_m, defined as [91]

$$H_\mathrm{m} = \int_V \mathbf{A}\cdot\mathbf{B}\,\mathrm{d}V, \tag{3.5}$$

where $\mathbf{A}$ is the generating vector potential for $\mathbf{B}$. This simplified formula applies to *closed* volumes, where the entire magnetic field structure is known. For solar and stellar applications, however, where magnetic structures permeate a photospheric boundary and are unknown under it, equation (3.5) bears no physical meaning. For this reason, Berger & Field [92] introduced a *relative* magnetic helicity in which one subtracts from the overall helicity of equation (3.5) the helicity of the vacuum magnetic field $\mathbf{B_p}$. This gives rise to a relative helicity $H_{\mathrm{m(rel)}}$ given by

$$H_{\mathrm{m(rel)}} = \int_V (\mathbf{A}+\mathbf{A_p})\cdot(\mathbf{B}-\mathbf{B_p})\,\mathrm{d}V, \tag{3.6}$$

where $\mathbf{A_p}$ is the generating vector potential for $\mathbf{B_p}$. Equation (3.5) ensures that $|H_{\mathrm{m(rel)}}| \to 0$ for $\mathbf{B} \to \mathbf{B_p}$. In addition, it has been shown analytically [93] and numerically [94] that the relative magnetic helicity is also a topological invariant for highly conductive magnetized plasmas, namely, plasmas with a high magnetic Reynolds number and a low-β parameter, such as the solar corona.

The non-conservation of magnetic energy vis-á-vis the conservation of the (relative) magnetic helicity in solar eruptions generates an immediate constraint: a given magnetic structure (say, a solar AR) *cannot* return to potentiality unless it finds a way to expel its magnetic helicity. Only a zero current density implies a zero relative helicity, which cannot be the case in an already helical (dextral [$H_{\mathrm{m(rel)}} > 0$] or sinistral [$H_{\mathrm{m(rel)}} < 0$]) confined magnetic structure (figure 4). A relevant question in this situation is how much free magnetic energy *at a minimum* can a magnetic structure with a *given* relative magnetic helicity carry. This theoretical question has been answered by Taylor

[95,96] for laboratory plasmas, but without loss of generality: the linear force-free approximation $\mathbf{J}=\alpha\mathbf{B_c}$ with constant-α ($\nabla\alpha=0$ in V) is this minimum-energy field. One may linearly relate E_m due to $\mathbf{B_c}$ and $H_{\mathrm{m}_{(\mathrm{rel})}}$ for linear force-free fields (e.g. [97]) and take this E_m as the minimum possible for a given $|H_{\mathrm{m}_{(\mathrm{rel})}}|$. Whether this minimum is tenable for the solar corona, however, is a longstanding matter of debate [98–100].

The above theoretical construction has led to pioneering works about the root cause of CMEs: these large-scale solar eruptions are a necessity for the Sun to relax from the excess magnetic helicity it accumulates in its atmosphere [101–104]. When decayed ARs fade away from the photosphere back to the solar interior, they should carry little or no helicity, as returning to below the photosphere with substantial amounts of helicity (and hence currents) violates entropy arguments. Therefore, over the billions of years of solar magnetic activity, an infinite amount of helicity would have been accumulated in the solar atmosphere, where free magnetic energy is constantly released to power the observed dynamics and to keep the corona hot. A counter-argument to bodily expulsion of magnetic helicity is helicity *annihilation*, apparently at work in some numerical models (e.g. [105]), that relies on the fact that helicity is a signed quantity, so it can be left- or right-handed. A magnetic reconnection of oppositely helical magnetic structures can lead to helicity cancellation or annihilation. While this notion is mathematically possible, it is challenged by the observed prevalence of opposite magnetic helicity signs in the northern and southern solar hemispheres [102] that is irrespective of the solar cycle [106], hence the reversal of solar magnetic poles, and is found to be due to the (equally unaffected by solar cycles) solar differential rotation [107]. If helicity annihilation is not the principal way for the Sun to relieve itself from its excess helicity, then expulsion of helical magnetic structures in the form of CMEs is the only known (and viable) way, not only for the Sun but, generally, for magnetically active, flaring stars [108].

So far, we have dealt almost exclusively with magnetic helicity. However, helicity, in general, is a topological property that quantifies the twist and the writhe of any divergence-free (i.e. closing on itself) vector field $\mathbf{b}$, viewed as the volume integral of the density $\mathbf{a}\cdot\nabla\times\mathbf{a}$ of its generating vector potential, $\mathbf{a}$. As such, there is *current* helicity, with density $\mathbf{B}\cdot\nabla\times\mathbf{B}$, as well as *kinetic* helicity, with density $\mathbf{u}\cdot\nabla\times\mathbf{u}$. In the former case, the magnetic field is viewed as the generator of the electric current density $\nabla\times\mathbf{B}$, while in the latter case the velocity field is viewed as the generator of the vorticity $\nabla\times\mathbf{u}$. Both have found applications to the Sun, for example, via [102,109,110] for the current helicity and via [111,112] for the kinetic helicity. However, all these helicity realizations invariably suffer from the lack of knowledge of the volume helicity density in actual solar observations. The likely exception is the kinetic helicity in the solar interior that is inferred via helioseismology observations at multiple depths in the convection zone. Therefore, without simplifying assumptions it is untenable to correlate between the different helicity expressions or even to evaluate each of them separately. For significant efforts on this objective, see [113,114].

Two notable exceptions to these severe limitations are, first, that the relative magnetic helicity, along with the magnetic energy, can be consistently inferred by the Poynting theorem in the photospheric boundary and, second, that magnetic and current helicity, along with the magnetic energy can, at least, be correlated in Fourier space.

The Poynting theorem for the magnetic energy (e.g. [115]) evaluates the energy rate crossing the photospheric boundary S by means of the photospheric flow field, namely

$$\frac{\mathrm{d}E_\mathrm{m}}{\mathrm{d}t}=\frac{1}{4\pi}\int_S\mathbf{B}\times(\mathbf{u}\times\mathbf{B})\cdot\hat{\mathbf{n}}\,\mathrm{d}S. \tag{3.7}$$

The above equation can be practically split into two terms, as follows:

$$\frac{\mathrm{d}E_\mathrm{m}}{\mathrm{d}t}=-\frac{1}{4\pi}\int_S\mathbf{u_t}\cdot\mathbf{B_t}B_n\,\mathrm{d}S+\frac{1}{4\pi}\int_S B_t^2u_n\,\mathrm{d}S, \tag{3.8}$$

where $\mathbf{B_t}$, $\mathbf{u_t}$ are the tangential components of $\mathbf{B}$ and $\mathbf{u}$, respectively, in the photosphere and u_n is the normal component of $\mathbf{u}$. The first term relates loosely to tangential, proper or peculiar—in

case of ARs—motions, while the second term correlates with the emergence of magnetic flux and the overall energy it carries.

The Poynting theorem can be extended to magnetic helicity, as well (e.g. [115,116]), yielding

$$\frac{\mathrm{d}H_\mathrm{m}}{\mathrm{d}t} = 2\int_S \mathbf{A_p}\times(\mathbf{u}\times\mathbf{B})\cdot\hat{\mathbf{n}}\,\mathrm{d}S, \tag{3.9}$$

and can be practically split into two terms, namely

$$\frac{\mathrm{d}H_\mathrm{m}}{\mathrm{d}t} = -2\int_S \mathbf{u_t}\cdot\mathbf{A_p}B_n\,\mathrm{d}S + 2\int_S \mathbf{A_p}\cdot\mathbf{B_t}u_n\,\mathrm{d}S. \tag{3.10}$$

A geometrical argument by Démoulin & Berger [117] identified a redundancy in equation (3.10), yielding a magnetic helicity rate

$$\frac{\mathrm{d}H_\mathrm{m}}{\mathrm{d}t} = -2\int_S \mathbf{u}'\cdot\mathbf{A_p}B_n\,\mathrm{d}S, \tag{3.11}$$

where the velocity field $\mathbf{u}' = \mathbf{u_t} - (u_n/B_n)\mathbf{B_t}$ on this case can be approximated by the local correlation tracking (LCT) velocity (for detailed information on this and other photospheric velocity realizations, see [118] and references therein).

Application of the Poynting theorem, therefore, requires the full photospheric **B** and **u** vectors or, in case of equation (3.11), B_n and the LCT velocity $\mathbf{u}'$. Practical ways to infer the vacuum vector potential $\mathbf{A_p}$ on S have been published and applied successfully [119].

While the rates of magnetic energy and helicity (assumed to be the relative helicity in this case) via equations (3.8) and (3.10)–(3.11) can be inferred and correlated over certain time intervals, one lacks the information on the actual energy and helicity budgets. Indeed, the above rates have a starting point arbitrarily set to zero; previously existing energy and helicity are not taken into account. Integrating these rates over time will provide indicative budgets of both quantities, lacking a reference point unless the calculation starts from the very initial stages of the AR emergence.

As to investigations in Fourier space, Zhang and colleagues [120–122] used mean fields to elaborate theoretically on the spectra of magnetic energy, $\mathcal{E}_\mathrm{m}(k,t)$, magnetic helicity, $\mathcal{H}_\mathrm{m}(k,t)$, and current helicity, $\mathcal{H}_\mathrm{c}(k,t)$. They found these spectra to be power laws with indices $-5/3$, $-8/3$ and $-5/3$, respectively. They managed to apply the theoretical calculations to observed timeseries of AR vector magnetograms, evaluating the time variations of these spectra. Most importantly, though, they validated the theoretical *realizability condition* of [123] that constrains $\mathcal{E}_\mathrm{m}(k,t)$ and $\mathcal{H}_\mathrm{m}(k,t)$ as follows:

$$\mathcal{E}_\mathrm{m}(k,t) \geq \frac{k}{2}|\mathcal{H}_\mathrm{m}(k,t)|. \tag{3.12}$$

One may, then, define a lengthscale ℓ_m by integrating $\mathcal{E}_\mathrm{m}(k,t)$ over the wavenumber space to find that, at any given time t, the mean coronal energy and helicity density, $e_\mathrm{m}(t)$ and $h_\mathrm{m}(t)$, respectively, are correlated as

$$e_\mathrm{m}(t) \geq \frac{1}{2\ell_\mathrm{m}}|h_\mathrm{m}(t)|. \tag{3.13}$$

Since it corresponds to mean densities, equation (3.13) may not be extremely revealing. It is important, however, because it ensures consistency by providing a lower limit for the magnetic energy for a given magnetic helicity. This limit is that of the linear force-free approximation, posed by Taylor [95,96]. The equation stemming from (3.13) may appear linear; it is not, however. This is because the lengthscale ℓ_m relates to the instantaneous energy spectrum $\mathcal{E}_\mathrm{m}(k,t)$, so it is itself a function of time. A linear correlation between magnetic energy and magnetic helicity (densities or budgets) exists only in the linear force-free approximation (e.g. [97]).

Other attempts to calculate the relative magnetic helicity in an open volume permeated by a boundary include field-line helicity [124] or twist helicity [125]. For a review of relative helicity calculation methods, see [126].

As another partial remedy to multiple limitations, we briefly recount the analysis of Georgoulis *et al.* [127]. This was a nonlinear force-free generalization of the linear analysis of Georgoulis *et al.*

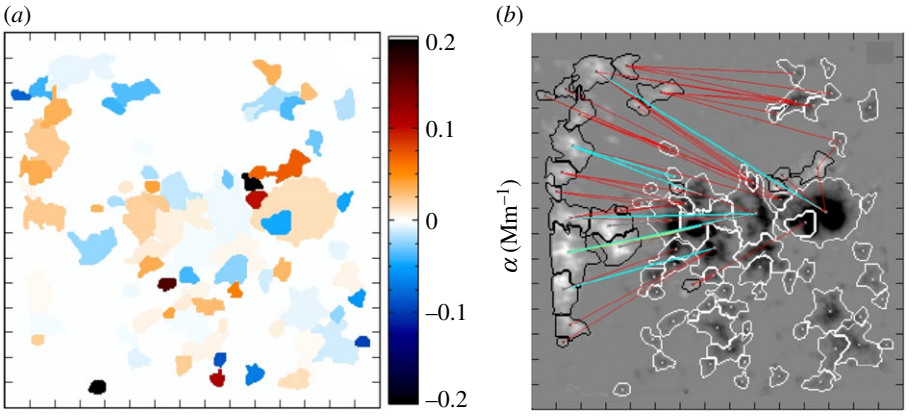

Figure 6. Indicative analysis steps followed to enable the evaluation of equations (3.14), (3.15). (*a*) Mean α-values of the partitioned photospheric flux map of the magnetogram shown on the right. (*b*) Photospheric projections of coronal magnetic connectivities on the magnetogram. The different segment colours indicate different connected fluxes for each flux tube. Only flux tubes closing within the field-of-view are represented. Magnetic field values in the right are saturated at ± 1 kG. Tick mark separation is 20". Solar north is up; west is on the right. Reproduced with permission from Georgoulis *et al.* [127].

[97]. In particular, Georgoulis *et al.* [127] used and extended the analysis of Démoulin *et al.* [128], in which a given magnetic structure can be thought of as a collection of N coronal magnetic flux tubes, each of them force-free but with different force-free parameters α_i and magnetic fluxes ϕ_i, $i \equiv \{1, \ldots, N\}$. Then a topological parsing or segmentation of the otherwise continuous photospheric flux distribution gave rise to T flux partitions, such as the example of figure 6. Over each partition, one knows both the magnetic flux and the mean α-value (figure 6*a*). Finally, a simulated annealing process aiming to connect opposite magnetic polarities and to minimize connection lengths, thus highlighting PILs, gave rise to a magnetic connectivity matrix φ_{pq} $(p, q \equiv \{1, \ldots, T\}, p \neq q)$, calculated over the partitioned photospheric flux, that provides the flux devoted to each connection between partitions (figure 6*b*). Each of these flux elements can be then considered as a coronal flux tube with flux $\phi_i = \varphi_{pq}$ and force-free parameter α_i, averaged between α_p and α_q and rooted in the flux-weighted centroids of the connected flux partitions p and q.

Assuming slender flux tubes, the problem of finding the relative magnetic helicity and free energy of the collection becomes then a discrete, geometrical one. In [127], the free magnetic energy budget E_c for a given photospheric magnetogram at a given time is

$$E_\mathrm{c} = Ad^2 \sum_{l=1}^{N} \alpha_l^2 \phi_l^{2\lambda} + \frac{1}{8\pi} \sum_{l=1}^{N} \sum_{m=1, l\neq m}^{N} \alpha_l \mathcal{L}_{lm}^{\mathrm{arch}} \phi_l \phi_\mathrm{m}, \tag{3.14}$$

while the instantaneous, simultaneous relative magnetic helicity $H_{\mathrm{m}_{(\mathrm{rel})}}$ is

$$H_{\mathrm{m}_{(\mathrm{rel})}} = 8\pi Ad^2 \sum_{l=1}^{N} \alpha_l \phi_l^{2\lambda} + \sum_{l=1}^{N} \sum_{m=1, l\neq m}^{N} \mathcal{L}_{lm}^{\mathrm{arch}} \phi_l \phi_\mathrm{m}. \tag{3.15}$$

In equations (3.14), (3.15), A and λ are known scaling constants, while d is the length element, substituted by the pixel size in case of observed photospheric magnetograms. The geometrical parameter $\mathcal{L}_{lm}^{\mathrm{arch}}$ is determined by the relative position of the flux-tube footpoints, needed to calculate the *mutual* terms of energy and helicity. The first terms of the rhs of equations (3.14), (3.15) correspond to the *self* terms of energy and helicity, respectively, that are due to the (force-free) electric current density estimated along the flux tubes.

Equations (3.14), (3.15) partially alleviate the lack of knowledge of the coronal magnetic field, providing consistent expressions for the *instantaneous* free magnetic energy and relative

magnetic helicity. For timeseries of magnetograms, one obtains pseudo-timeseries of free-energy and relative-helicity budgets, with values closely spaced in time but independent from each other. These equations further ignore additional helicity and energy terms due to braiding between flux tubes, which cannot be known unless the coronal magnetic configuration is known precisely, as well as some induction-related terms in the free energy, due to the interaction between current-carrying flux tubes [128]. Equations (3.14), (3.15), in view also of the previous discussion, will be useful in describing the evolutionary course of ARs towards eruptions in the following.

4. The course toward coronal mass ejections

We mentioned in §3 that most ARs seem to have a prevalent sense of magnetic (and current) helicity, either left- or right-handed, that was theoretically asserted by Seehafer [109] and was first shown observationally by Pevtsov *et al*. [102]. Further observational analyses [129–132] aligned to this finding for eruptive ARs. Later on, using equations (3.14), (3.15), Tziotziou *et al.* [133] produced an 'energy-helicity' diagram correlating the nonlinear force-free magnetic energy and relative magnetic helicity of numerous ARs, each studied at multiple times (figure 7).

The plot of figure 7 implies a nearly monotonic dependence of free energy and relative helicity magnitude, with eruptive ARs statistically occupying its higher end–some exceptions are seen and discussed in [133]. The robustness of this diagram, even using quiet-Sun magnetograms and MHD simulations that did not rely on equations (3.14), (3.15), was demonstrated by Tziotziou and colleagues [37,134,135]. A case study of this was also the investigation of Patsourakos *et al.* [136], where it was found that the exceptionally eruptive NOAA AR 11429 (figure 2) had equally exceptionally large values of free energy and relative helicity of a given (left-handed) sense.

The relevant question to address, therefore, is how eruptive ARs manage to accumulate large amounts of free energy and relative helicity to power eruptions. An interpretation has been offered by Georgoulis *et al*. [137]. In this work, that is further discussed extensively by Georgoulis [25], it was found that *non-neutralized* (i.e. net) electric currents in ARs appear *exclusively* along intense PILs. The effect also leads to a prevalent, coherent sign of these currents per magnetic polarity that gives rise to a prevalent sign for the relative helicity. In this sense, ARs with strong, sheared PILs tend to have a consistent velocity shear orientation leading to a consistent non-neutralized current sign and a resulting prevalent relative helicity sense. In [137], an extensive analysis over the existence of non-neutralized currents in solar ARs, strongly debated in longstanding works by Parker [85] and Melrose [138], resulted in arguably the first unambiguous detection of net currents in the solar photosphere, along with the finding that these currents can only exist along intense PILs.

Injection of net electric currents in the corona greatly enhances the free magnetic energy associated with strong PILs, sufficient to power major eruptions. It comes at no surprise, then, that eruptive ARs in figure 7 almost invariably exhibit conspicuous PILs. Another key aspect of figure 7 is the empirical finding of certain free-energy and relative-helicity limits that eruptive ARs exceed. For relative helicity, this limit is approximately $2 \times 10^{42}\,\mathrm{Mx}^2$, which is believed to be a typical CME helicity content [107,139]. Albeit from a different perspective, this finding aligns with that of [140] regarding an upper pre-eruption helicity bound for a given boundary condition. For free energy, this limit is approximately 4×10^{31} erg that is a typical energy content of a flare of GOES class M and above ([133] treated as 'eruptions' eruptive flares of class M and above, which is consistent with the shown free-energy limit in figure 7).

If the efficient accumulation of magnetic free energy and helicity of a certain sign above PILs is facilitated by non-neutralized electric currents, then it becomes relevant to interpret this effect physically. In [137], this was attributed to the Lorentz force. Indeed, the azimuthal component of the Lorentz force along the PIL in cylindrical geometry (r, φ, n) with the (r, φ)-plane on the photosphere is

$$F_\varphi \simeq \frac{B_n}{4\pi}\left(-\frac{1}{r}\frac{\partial B_n}{\partial \varphi} + \frac{\partial B_\varphi}{\partial n}\right). \tag{4.1}$$

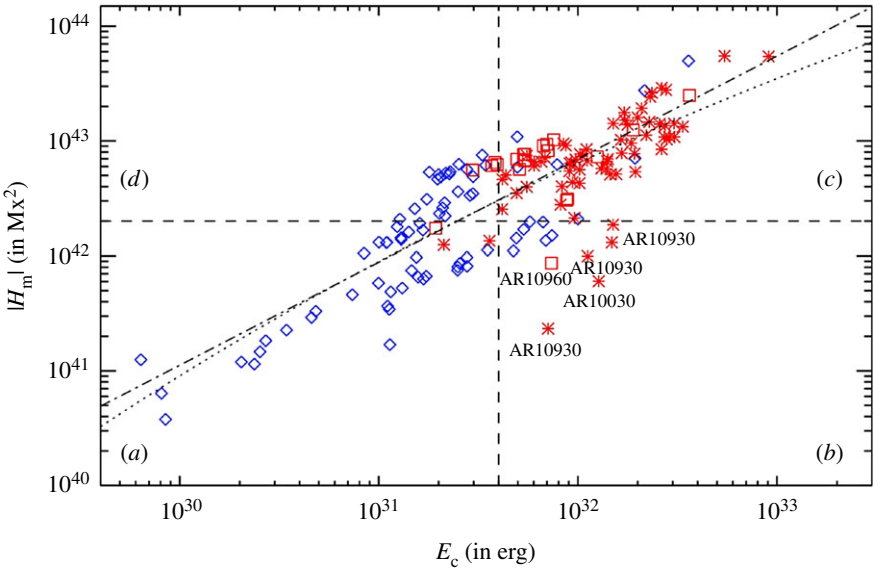

Figure 7. Scatter plot of the relative helicity magnitude $\left|H_{m_{(rel)}}\right|$ as a function of the free magnetic energy E_c for 162 vector magnetograms of several solar ARs at different evolutionary stages. Red symbols indicate eruptive ARs, while blue symbols indicate non-eruptive ones. Dashed horizontal and vertical lines show empirically inferred limits of free energy and relative helicity for ARs to be eruptive, while the dotted and dash-dotted lines show the least-squares best-fit curves using two different regression approximations. Reproduced with permission from Tziotziou *et al*. [133].

The above equation represents a purely tension force approximated for the edges of the photospheric flux footprints, where sheath currents separate strong magnetic-flux patches by the surrounding quiet Sun, as per [137] and references therein. In case a strong PIL is lacking, undisturbed, isolated polarities may exhibit an azimuthal symmetry ($\partial/\partial\varphi \sim 0$). Moreover, the vanishing B_n at the edges of flux patches in this case gives rise to an insignificant tension, $F_\varphi \sim 0$. However, in case of strong PILs, the sheath current pattern is disrupted along the PILs; therefore, azimuthal symmetry is lost. Moreover, except precisely on the PIL where $B_n = 0$ (see, e.g. figure 2), $|B_n| \gg 0$ and of opposite sign in the two sides of the PIL. This gives rise to a strong, oppositely oriented F_φ in the two sides of the PIL, as shown schematically in figure 9 of [137].

For strong PILs, the magnetic field strength is well above the photospheric equipartition value of approximately 1 kG, so $\beta < 1$ already in the photosphere. This is our quantification of a 'strong', or 'intense', photospheric PIL. It means that the plasma is magnetized and can be forced to motion by the Lorentz force even at photospheric levels. In [137], the velocity shear observed invariably along PILs is attributed to the tension force F_φ of equation (4.1), for the MHD equation of motion to be fulfilled. For reasons detailed in that work, a coherent sign for the cross-field non-neutralized currents will give a consistent orientation of F_φ, that will further give a consistent shear orientation, as observed. This effect, similar to the effect of sunspot rotation (e.g. [141]), will give a prevalent magnetic helicity sign to the AR. The persistent shearing along strong PILs, often lasting several days, will generate immense amounts of free magnetic energy and helicity with a preferred sign, hence the large amounts of helicity for eruptive ARs, as per figure 7. Furthermore, when certain thresholds are crossed, the structure cannot remain contained any longer, giving rise to an eruption, possibly via multiple triggers (§5). Since the AR will not return to potentiality with just one eruption (typically even the largest flares tend to release up to approximately 10% of the available free energy in the host regions (e.g. [142]), while CMEs up to approximately half of the available helicity (e.g. [116,143])), an eruptive AR will host a series of CMEs until complete relaxation happens. Repeated eruptions are also a trait of intensely eruptive ARs.

It is important to emphasize that the above process is fuelled by flux emergence, which enhances the magnetic pressure and hence the well-known converging motions toward PILs, in an effort of the emerging structure to expand further.

It should be further noted that attribution of shearing motions to the Lorentz force was also a conclusion of Manchester and colleagues [144–147]. In addition, the exclusive appearance of non-neutralized currents along PIL was also a key result of Török *et al.* [148], using three-dimensional MHD models, although these authors stopped short of attributing this effect to the Lorentz force.

But if the Lorentz tension force starts acting as soon as a strong ($\beta < 1$) photospheric PIL is formed, and will not cease until there is no flux emergence, so no more strong PIL(s) and net currents (as is the case in ARs well into their decay phase), then the big physical picture points to an *irreversible* evolution in this minority class of intensely eruptive ARs: a strong PIL formation in the initial AR stages of evolution can only relate to the sub-surface structure of the buoying flux-tube progenitor (e.g. [35,149]). In these uncommon cases, compared to the thousands of 'flareless' ARs that appear, evolve and disappear within a typical solar cycle, the course toward eruptions seems sealed even before these ARs emerge. It starts developing soon (within hours or tens of hours) after they emerge, mainly in the course of flux-emergence phase but also beyond that, as the PIL weakens gradually, so that the AR can release the PIL-associated remnants of free energy and shed away the magnetic helicity that sustains this energy.

This irreversibility remains to be conclusively shown by observed data analyses. A conclusive result would be the visualization of the Lorentz force along the PILs in eruptive ARs. If the Lorentz force orientation is in acute-angle relation with the observed shear, this would be supporting evidence to the theoretical picture described above. If not, then shear should be counteracting the Lorentz force. We argue that the latter would complicate the interpretation of the MHD equation of motion. The task of calculating the Lorentz force properly is severely hampered by the lack of magnetic field information at different heights in and above the photosphere, which inhibits the complete calculation of the electric current density $\mathbf{J}$ – and hence of the Lorentz force $\mathbf{F} \sim \mathbf{J} \times \mathbf{B}$ – in the photosphere. These limitations have so far resulted in only partial or dimensional Lorentz force calculations, in view of simplifying assumptions (e.g. [150,151]), that by no means reach such level of detail as to infer the orientation of the photospheric Lorentz force vector. It suffices saying, however, that efforts to bring this pursuit to a closure are underway.

A further significant ramification of the above picture of forced PIL evolution is a pattern of helicity noted when an eruptive AR is observed from its initial evolutionary stages: in [37], intensely eruptive NOAA AR 11158 was observed by SDO/HMI for a period of several days. Evaluating equations (3.14), (3.15) allowed the correlation of the mutual and self-energy and helicity terms as the AR evolved (figure 8). One notes a close correspondence, albeit via a hysteresis, of the self over the mutual term of magnetic helicity, with mutual helicity preceding self-helicity by up to approximately 12 h for the first approximately 48 h of AR evolution. The respective free energy terms show a much more loose and less consistent correlation. This was interpreted by means of the fundamental conservation property of magnetic helicity, as opposed to the non-conservation of magnetic energy: helicity efficiently converts from mutual to self, giving rise to a progressively more self-helical (i.e. twisted and/or writhed) pattern of the AR magnetic structure. On the contrary, significant free energy is lost in the course of this conversion, although the overall budgets of energy and helicity in the AR are increasing due to the intense emergence of non-potential flux. This points to a resistive process, happening mostly along PILs, meaning that the substantial mutual helicity of the emerging AR is translated to self-helicity via numerous magnetic reconnection episodes. It is, of course, well known that small-scale magnetic reconnection is routinely at work along strong PILs even in non-flaring intervals. Besides releasing energy, Tziotziou *et al.* [37] made clear that this process leads also to progressively more self-helical structures. These results have been confirmed in other cases of ARs observed since initial emergence by SDO/HMI, with the relevant presentation efforts underway.

The assessed progressive self-helical structure formation above PILs, however, is in direct agreement with (i) the formation of filament channels (§2), and (ii) the remarkable, well-observed pre-eruption flux-rope formation triggered by confined flaring, first reported by Patsourakos *et al.*

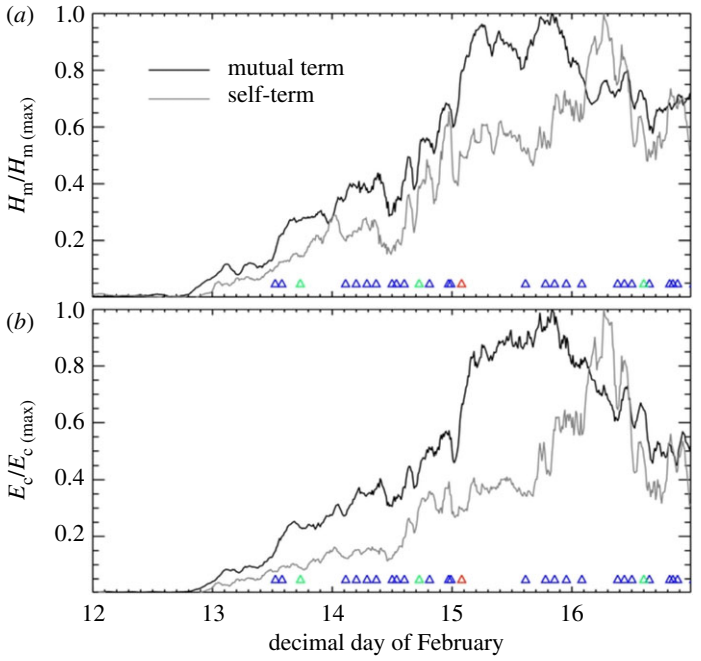

Figure 8. Evolution of the normalized mutual and self-terms of (*a*) relative magnetic helicity and (*b*) free magnetic energy in NOAA AR 11158 for a five-day period in February 2011. The triangles indicate the onset times of flares triggered in the AR, with GOES C-, M- and X-class events denoted by blue, green and red, respectively. From Tziotziou *et al.* [37].

[64] (figure 4) and further corroborated by Chintzoglou *et al.* [27] and Nindos *et al.* [63]. This may eventually provide valuable clues toward a more robust interpretation of CME triggering (see §5, below): sheared arcades may lead to eruptions without the requirement of a pre-eruption flux rope if there is at least one null point in the overlying corona—if not, however, a pre-eruption flux rope may need to be formed first. These seemingly competing eruption mechanisms by no means invalidate our proposed physical picture of a vital role of the free energy *and* the relative helicity: sheared arcades are structures with substantial mutual helicity that may, or may not, manage to convert to significant self-helicity prior to eruptions, depending on the existence of an overlying coronal null. If this exists, the expanding, increasingly sheared arcade will be destabilized by means of a so-called *breakout* reconnection (see §5 below); otherwise, the arcade will be allowed to evolve into a pre-eruption flux rope.

5. Coronal mass ejections triggering and driving mechanisms

The mechanisms involved in the course toward eruptions are often dubbed *triggers* and *drivers* of eruptions (see [7]). Triggers are mechanisms that can initiate the eruption but cannot by themselves produce a CME, while drivers are mechanisms responsible for the acceleration and expansion of the erupting magnetized plasma. Both have been the subject of extensive research. A common approach involves the development of CME initiation models, either analytical or—more often—numerical, that treat both the trigger and the driver. Instead of an exhaustive discussion of available models, we will highlight the most important trends and schools of thought in the subject, along with some notable alternatives. The reader is referred to the several excellent reviews of, e.g. [7,14,24,32,33,152,153], for more details.

Virtually all models are formulated as initial boundary-value problems, involving a system of differential equations that correspond to a single-fluid MHD, a set of boundary conditions that are well constrained by observations (see §2) and an initial state. All models have limitations

because (i) the use of the MHD approximation does not allow treatment of kinetic phenomena, (ii) the coronal magnetic field is not known and therefore the initial state is determined on an *ad hoc* basis, and (iii) there are computer power limitations that inhibit the complete coverage of the relevant spatial dynamical range, from reconnection scales in the low solar atmosphere to heliospheric scales of CME propagation. Despite these shortcomings, the available models are still our most valuable tool towards testing candidate eruption mechanisms.

Most models fall under the 'storage and release' category, i.e. they assume that the free magnetic energy required for the eruption is quasi-statically accumulated in the corona and then rapidly released as the eruption takes place (but see the review by Klimchuk [24] for a discussion of alternative paradigms). In these models, the pre-eruptive, core magnetic configuration is current-carrying and could be either a flux rope or a sheared magnetic arcade, with a potential ambient field surrounding the core. However, in all models the erupting structure is a flux rope; if it is not included in the pre-eruption configuration, it is formed by magnetic reconnection in the course of the eruption.

Several processes have been used for the formation of the eruptive magnetic structure and the supply of its free magnetic energy. The use of shearing (e.g. [154–156]) or twisting (e.g. [157–159]) motions is a natural choice for models employing a sheared magnetic arcade. In case of flux ropes, flux cancellation after emergence (e.g. [40,160–162]) or emergence of the flux rope itself from the convection zone to the corona (e.g. [163–166]) is invoked.

Usually, CME drivers, i.e. models of CME initiation, are categorized as either ideal or resistive. This classification is equivalent to the classification of models with respect to their pre-eruptive magnetic configuration. In ideal models, reconnection is not the driver of the eruption, but it may facilitate it by removing the overlying field (e.g. see [167,168]). It is also possible that reconnection is invoked to create the initial state that will be destabilized and erupt ideally at a later stage. In resistive models, reconnection is the fundamental driver of the eruption, responsible for its onset and growth in time, as well as for the formation of the flux rope during the eruption.

In ideal models, the coronal magnetic field reaches a critical point where a loss of equilibrium (also known as a 'catastrophe') or a loss of stability occurs, leading to the eruption. Loss-of-equilibrium models (e.g. see [169–172]) show that as a result of various triggering processes (controlled by the properties of either the flux rope or the overlying field or even by flux emergence) there is a critical point where a jump in the quasi-static evolution curve of the flux rope height may appear. The jump yields the formation of a vertical current sheet underneath the flux rope. If reconnection is invoked in the current sheet, the flux rope may not be able to achieve equilibrium and will rise in the corona as a CME.

The main contenders of ideal loss-of-equilibrium models are the torus and the kink instabilities (see [173] and references therein). The torus instability, the catastrophe model's equivalent MHD description [174], arises in a plasma ring with toroidal current and stability maintained by an external magnetic field perpendicular to the axis of the torus. This gives rise to a downward force that balances both upward Lorentz self-force and the pressure gradient force of the ring. This equilibrium is unstable against expansion if the external field decreases fast enough in the direction of the major axis of the torus. Usually, the rate at which the field decreases with height is quantified by a so-called decay index $n = -(z/B)(\partial B/\partial z)$, where B is the magnetic field strength and z the height above the photosphere. It has been found that a flux rope may erupt if the parameter n associated with the ambient overlying field exceeds a critical threshold ranging between 1.1 and 2 [174–176]. A key property of the torus instability is that its threshold is independent of the current stored into the core field. Furthermore, unlike the kink instability (see below) it never saturates completely; therefore, it may operate at any height in the corona. Simulations of eruptions driven by the torus instability [177] have shown that the acceleration profiles of the resulting CMEs depend on the values of n; large (small) values associated with a quadrupolar (bipolar) magnetic configurations yield fast (slow) CMEs, which is consistent with observations (§1).

The kink instability is a current-driven, ideal MHD instability associated with the $m = 1$ kink mode. It may occur in a flux rope if the twist of the field lines exceeds a critical value (e.g.

[173]). The instability reduces the bending of the field lines which results in the decrease of the magnetic energy of the flux rope as well as in the conversion of some of its twist to writhe via rapid untwisting motions. Such helical deformations are often observed in erupting prominences (e.g. [104]) which makes the kink instability an attractive CME driver in case the low-coronal progenitors show a helical shape. However, it has also been found (see [178]) that the kink instability saturates quickly, which could make it more appropriate for the interpretation of failed eruptions (e.g. [84]). But the kink instability may facilitate some eruptions by lifting the flux rope into a height range where the torus instability can take over.

Depending on the height at which reconnection occurs, there are two sub-classes of resistive drivers, namely the tether-cutting model and the breakout model. The former (e.g. [83]) employs a bipolar magnetic configuration; reconnection occurs below the sheared core of the magnetic configuration and transforms much of the overlying flux into twisted field lines that surround the initial core configuration. Therefore, the reconnection reduces the restraining tension force exerted by the overlying field. This mechanism is explosive because as reconnection progresses the tension force weakens, facilitating an impulsive rise of the erupting structure. Tether-cutting has been a successful eruption driver in axisymmetric [154,179] and 2D/2.5D [157] MHD simulations, but it has been argued (see [153] and references therein) that it cannot be the main driver of eruptions in full 3D geometries. However, several authors (see [33] and references therein) interpret observed eruptions in terms of tether-cutting. These observations include flare brightenings as well as weak precursor transients occurring prior to the eruption at the AR core.

The breakout model [180] requires a quadrupolar magnetic configuration with a coronal null point that lies between the central sheared magnetic field lines and the overlying field. The flux rope that will eventually erupt forms due to reconnection below the sheared arcade. Unlike tether-cutting, reconnection also occurs at the null point above the core field, which leads to the removal of the overlying magnetic field and to an explosive outward expansion. As in the tether-cutting mechanism, breakout can establish a 'feedback loop' leading to an eruption. The model has been successfully extended to 2.5D [181–183] and 3D simulations [184]. Observational evidence in favour of the breakout model includes eruptions occurring in multipolar ARs with active coronal nulls (e.g. [185,186]), as well as the detection of small-scale UV brightenings taking place away from the AR core (e.g. see [187] and references therein).

A notable alternative to the storage-and-release models has been developed by Chen and colleagues [188–192]. The initial configuration of this model is a flux rope whose footpoints extend below the photosphere. The flux rope is driven away from equilibrium by the injection of poloidal magnetic flux that enhances the so-called hoop force acting on it as a consequence of the self fields. The energy release stems from the energy deposited by the injected field in shorter timescales than the storage-and-release would require. The most attractive feature of this model is its ability to reproduce the observed trajectories of some CMEs by suitably adjusting the amount of poloidal flux injection (see [191,193]). However, the model has been criticized on the grounds that it requires upflows well in excess of those observed in the photosphere to account for nominal helicity and energy budgets of the flux rope [194].

6. Conclusion

In this review, we aimed to describe the fundamental causes, consequences, drivers and triggers of AR solar eruptions, from the appearance of ARs to the initial stages of CMEs. The review discusses the main findings of influential works in these topics. In addition, it aims to complement the fundamental, undeniable role of free magnetic energy in powering solar eruptions with an equally important and fundamental physical parameter: the magnetic helicity, specifically the element of it pertaining to electric currents (relative helicity). In a loose analogy, if the source of CMEs is the free magnetic energy, the engine of CMEs is the magnetic helicity, as per the reasoning followed throughout the review.

CMEs would hardly exist without magnetic helicity, as has been conjectured theoretically, shown analytically and demonstrated numerically by the resulting helical flux-rope morphology

of virtually all CMEs at their initial stages of evolution. Had magnetic helicity not played this role, facilitated by its fundamental conservation property for highly conductive plasmas, dissipation of the Sun's electric currents and eventual relaxation of the solar magnetized atmosphere would have most likely been achieved by a self-similar spectrum of flares of all energies ([195] and references therein), from possible nanoflares [196] to the largest observable events. Dissipation of energy in the Sun's corona is quasi-steady, to the extent that if the corona's energy provision was switched off, the hot, million-Kelvin solar atmosphere would disappear within tens of minutes. The free energy of the corona cannot be dissipated altogether, however, due to the presence of the conserved helicity. A continuous increase of helicity without hope for complete dissipation, or annihilation, would seemingly lead to a paradoxical infinity of helicity and free energy in the solar corona, imposed by the well-known hemispheric helicity preference. Avoiding this unphysical situation is what makes CMEs necessary, from ARs to the quiet Sun. We discuss a likely path or procedure in this review that, however, focuses on ARs, given that major eruptions are triggered exclusively in them.

Major solar eruptions, i.e. eruptions composed of major flares and fast CMEs, are hosted by a slim minority of solar ARs. The single distinguishing feature of this class of ARs is their intense magnetic PILs, observed in the photospheric interface and assumed to topologically extend upward to the corona. This review uses the convention $\beta < 1$ in photospheric PILs (that is, magnetic fields higher than the local equipartition value) to distinguish 'intense' or 'strong' PILs from much weaker, unsheared PILs forming invariably in all ARs. Strong PILs constitute a very efficient means of accumulating free energy and corresponding relative helicity. It appears that the crossing of certain thresholds for free energy and relative helicity paves the way for at least one, but typically a series, of eruptions in these ARs. Remarkably, the threshold for CMEs is the typical CME helicity of a few times 10^{42} Mx^2 (figure 7), as has been independently inferred, both numerically [139] and observationally [107]. This could lead to the conclusion that an AR may give a CME relatively shortly after it has accumulated the helicity for it, although in reality the magnetic helicity of eruptive ARs is often well above this limit, which can account for series of CMEs these ARs can host.

The accumulation of magnetic helicity above intense PILs contributes, along with flux emergence, to the expansion of the magnetic structure characterized by the PIL. Most importantly, it dictates the resistive progression toward a pre-eruption flux rope, demonstrated conclusively in a number of works. The most plausible initial configuration associated with a strong PIL is, indeed, a sheared magnetic arcade that could also account for the invariable formation of filament channels aligned with the PILs. Sheared arcades may not have significant self-helicity (twist and writhe), but they have substantial mutual helicity due to the interaction of numerous emerging current-carrying flux tubes [128]. This helicity is continuously transformed to self-helicity via small-scale magnetic reconnection that is a common occurrence along PILs. The resulting feature is an increasingly self-helical, expanding—due to its increasing magnetic pressure—configuration, facilitated by flux emergence. The instability has multiple candidate drivers and can be triggered before the formation of an observable flux rope or after it, but it will occur, nonetheless. The notable, intriguing counterexample of NOAA AR 12192 that hosted a large number of confined flares (e.g. [197]), possibly due to properties of the overlying magnetic field, eventually gave way to a single CME [198] before rotating to the far side. Substantial discussion has been already devoted to this exceptional target that warrants further investigation.

Intense PILs being a feature inherited to some ARs from their ascension through the convection zone, the facilitator of the eruption triggers (namely, frequent small-scale magnetic reconnection and mutual-to-self-helicity conversion) is the velocity and magnetic shear, invariably acting along intense PILs. While this remains to be shown conclusively, this report highlights an argument put forth by some previous works that the observed shear is due to the action of the Lorentz tension force acting along these exceptional PILs, at least as long as flux emergence lasts. Tension force can move the plasma as the magnetic field strength exceeds the equipartition value in the photosphere and may account for the velocity shear. Shear flows further modulate the current-density pattern

along PILs leading to magnetic shear, that is, increased stress and subsequent enhancements of electric current density and free energy.

However, if the formation of a strong, shear-ridden photospheric (and atmospheric, by extension) PIL is mainly a matter of sub-photospheric characteristics of some ARs, then one sees a certain irreversibility in this physical course: ARs that are destined to carry much of the solar helicity generated in the tachocline, at the base of the convection zone, are also destined to shed this helicity into the heliosphere before fading away. Eruptions become inevitable as soon as their photospheric PILs acquire field strengths above the equipartition value.

The realism of the above interpretation of CMEs relies on the currently unknown orientation of the Lorentz force in the photosphere. The photospheric Lorentz force vector, however, cannot be inferred by single-height, photospheric observations alone. If no assumptions or modelling is involved, one would need multi-height magnetic field observations to achieve knowledge of the 3D magnetic structure above the photosphere, which would ideally allow the complete calculation of both the electric current density and the Lorentz force vectors. Obtaining the 3D magnetic field by observations is highly non-trivial, however, as discussed by multiple authors (e.g. [199,200] and references therein). This said, the Daniel K. Innue Solar Telescope (DKIST) in the US and the European Solar Telescope (EST) in Europe, among other, smaller ground-based facilities, promise to provide this currently untenable knowledge, in local solar scales. If modelling and/or simplifying assumptions are employed to infer the photospheric Lorentz force vector from observed photospheric vector magnetograms, on the other hand, these approximations cannot be force-free. Yet we feel that a definitive answer to this open question will stem from future solar magnetographic efforts.

Concluding, we caution that, to fully understand the intrinsic details of solar eruption triggering and driving, one ideally needs three-dimensional, full-vector magnetographic observations with at least the present photosphreric accuracy at the *actual* lower boundary of solar eruptions, namely, a few Mm above the photosphere. The formation height of DKIST and EST magnetically sensitive spectral lines may be insufficient for this purpose and it is unclear whether this task will be feasible in the foreseeable future. As a result, we are restricted to using the photosphere as a *proxy* lower boundary for solar eruptions, in hopes that conclusions reached using science-grade photospheric (or future low-chromospheric) vector magnetograms have the validity and generality we need to understand, and ultimately predict, Earth-affecting solar transients.

Data accessibility. This article does not contain any additional data.

Authors' contributions. M.K.G., as the corresponding author, oversaw the writing of the entire manuscript and led the writing of §§3, 4. A.N. led the writing of §§1, 2 and 5. H.Z. contributed to all sections, also providing parts of the discussion. All authors contributed to the conclusion, §6. In addition, all authors read and approved the manuscript.

Competing interests. We declare we have no competing interests.

Funding. Part of the previously published, original work included in this review was supported by the European Union (European Social Fun-ESF) and Greek national funds through the Operational Program 'Education and Lifelong Learning' of the National Strategic Reference Framework (NSRF)-Research Funding Program: 'Thales. Investing in knowledge society through the European Social Fund'. H.Z. further acknowledges funding from the National Natural Science Foundation (NNSF) of China under project grant nos. 11673033, 11427803, 11427901 and Huairou Solar Observing Station, National Astronomical Observatories of China.

Acknowledgements. We acknowledge significant contributions by two anonymous referees in the presentation of ideas discussed in the manuscript and in several clarifications that improved its readability.

References

1. Webb DF, Howard TA. 2012 Coronal mass ejections: observations. *Living Rev. Solar Phys.* **9**, 3. (doi:10.12942/lrsp-2012-3)
2. Fletcher L *et al.* 2011 An observational overview of solar flares. *Space Sci. Rev.* **159**, 19–106. (doi:10.1007/s11214-010-9701-8)

3. Andrews MD. 2003 A search for CMEs associated with big flares. *Solar Phys.* **218**, 261–279. (doi:10.1023/B:SOLA.0000013039.69550.bf)
4. Yashiro S, Gopalswamy N, Akiyama S, Michalek G, Howard RA. 2005 Visibility of coronal mass ejections as a function of flare location and intensity. *J. Geophys. Res. (Space)* **110**, A12S05. (doi:10.1029/2005JA011151)
5. Hudson HS, Cliver EW. 2001 Observing coronal mass ejections without coronagraphs. *J. Geophys. Res. (Space)* **106**, 25199–25214. (doi:10.1029/2000JA904026)
6. Gopalswamy N, Mikić Z, Maia D, Alexander D, Cremades H, Kaufmann P, Tripathi D, Wang Y-M. 2006 The pre-CME sun. *Space Sci. Rev.* **123**, 303–339. (doi:10.1007/s11214-006-9020-2)
7. Green LM, Török T, Vršnak B, Manchester W, Veronig A. 2018 The origin, early evolution and predictability of solar eruptions. *Space Sci. Rev.* **214**, 46. (doi:10.1007/s11214-017-0462-5)
8. Mandrini CH, Pohjolainen S, Dasso S, Green LM, Démoulin P, van Driel-Gesztelyi L, Copperwheat C, Foley C. 2005 Interplanetary flux rope ejected from an X-ray bright point. The smallest magnetic cloud source-region ever observed. *Astron. Astrophys.* **434**, 725–740. (doi:10.1051/0004-6361:20041079)
9. Qiu J, Yurchyshyn VB. 2005 Magnetic reconnection flux and coronal mass ejection velocity. *Astrophys. J.* **634**, L121–L124. (doi:10.1086/498716)
10. Georgoulis MK. 2008 Magnetic complexity in eruptive solar active regions and associated eruption parameters. *Geophys. Res. Lett.* **35**, L06S02. (doi:10.1029/2007GL032040)
11. Sheeley Jr NR, Warren HP, Wang YM. 2007 A streamer ejection with reconnection close to the sun. *Astrophys. J.* **671**, 926–935. (doi:10.1086/522940)
12. Vourlidas A, Webb DF. 2018 Streamer-blowout coronal mass ejections: their properties and relation to the coronal magnetic field structure. *Astrophys. J.* **861**, 103. (doi:10.3847/1538-4357/aaca3e)
13. Vourlidas A, Lynch BJ, Howard RA, Li Y. 2013 How many CMEs have flux ropes? Deciphering the signatures of shocks, flux ropes, and prominences in coronagraph observations of CMEs. *Solar Phys.* **284**, 179–201. (doi:10.1007/s11207-012-0084-8)
14. Chen PF. 2011 Coronal mass ejections: models and their observational basis. *Living Rev. Solar Phys.* **8**, 1. (doi:10.12942/lrsp-2011-1)
15. Forbes TG *et al.* 2006 CME theory and models. *Space Sci. Rev.* **123**, 251–302. (doi:10.1007/s11214-006-9019-8)
16. Simões PJA, Fletcher L, Hudson HS, Russell AJB. 2013 Implosion of coronal loops during the impulsive phase of a solar flare. *Astrophys. J.* **777**, 152. (doi:10.1088/0004-637X/777/2/152)
17. Wang J, Simões PJA, Fletcher L. 2018 Unambiguous evidence of coronal implosions during solar eruptions and flares. *Astrophys. J.* **859**, 25. (doi:10.3847/1538-4357/aabc0e)
18. Howard T (ed.). 2011 Coronal mass ejections, *Astrophysics and space science library*, vol. 376.
19. Lara A, Gopalswamy N, DeForest C. 2000 Change in photospheric magnetic flux during coronal mass ejections. *Geophys. Res. Lett.* **27**, 1435–1438. (doi:10.1029/1999GL003666)
20. Sudol JJ, Harvey JW. 2005 Longitudinal magnetic field changes accompanying solar flares. *Astrophys. J.* **635**, 647–658. (doi:10.1086/497361)
21. Petrie GJD. 2016 Photospheric and coronal observations of abrupt magnetic restructuring in two flaring active regions. *Solar Phys.* **291**, 791–821. (doi:10.1007/s11207-016-0873-6)
22. Hudson HS, Fisher GH, Welsch BT. 2008 Flare energy and magnetic field variations. In *Subsurface and atmospheric influences on solar activity* (eds R Howe, RW Komm, KS Balasubramaniam, GJD Petrie). Astron. Soc. Pacific Conf. Ser., no. 383, p. 221.
23. Bi Y, Yang J, Jiang Y, Hong J, Xu Z, Qu Z, Ji K. 2017 The photospheric vortex flows during a solar flare. *Astrophys. J. Lett.* **849**, L35. (doi:10.3847/2041-8213/aa960e)
24. Klimchuk JA. 2001 *Theory of coronal mass ejections*. Geophysical Monograph Series, vol. 125. Washington, DC: American Geophysical Union.
25. Georgoulis MK. 2018 The ambivalent role of field-aligned electric currents in the solar atmosphere. In *Electric currents in geospace and beyond* (eds A Keiling, O Marghitu, M Wheatland). Geophysical Monograph Series, no. 235, pp. 371–390. Washington, DC: American Geophysical Union.
26. Schrijver CJ. 2007 A characteristic magnetic field pattern associated with all major solar flares and its use in flare forecasting. *Astrophys. J. Lett.* **655**, L117–L120. (doi:10.1086/511857)

27. Chintzoglou G, Patsourakos S, Vourlidas A. 2015 Formation of magnetic flux ropes during a confined flaring well before the onset of a pair of major coronal mass ejections. *Astrophys. J.* **809**, 34. (doi:10.1088/0004-637X/809/1/34)
28. Feynman J, Martin SF. 1995 The initiation of coronal mass ejections by newly emerging magnetic flux. *J. Geophys. Res. (Space)* **100**, 3355–3367. (doi:10.1029/94JA02591)
29. Chen PF, Shibata K. 2000 An emerging flux trigger mechanism for coronal mass ejections. *Astrophys. J.* **545**, 524–531. (doi:10.1086/317803)
30. Archontis V, Török T. 2008 Eruption of magnetic flux ropes during flux emergence. *Astron. Astrophys.* **492**, L35–L38. (doi:10.1051/0004-6361:200811131)
31. Mackay DH, Gaizauskas V, Yeates AR. 2008 Where do solar filaments form?: consequences for theoretical models. *Solar Phys.* **248**, 51–65. (doi:10.1007/s11207-008-9127-6)
32. Schmieder B, Aulanier G, Vršnak B. 2015 Flare-CME models: an observational perspective (Invited review). *Solar Phys.* **290**, 3457–3486. (doi:10.1007/s11207-015-0712-1)
33. Cheng X, Guo Y, Ding M. 2017 Origin and structures of solar eruptions I: magnetic flux rope. *Sci. China Earth Sci.* **60**, 1383–1407. (doi:10.1007/s11430-017-9074-6)
34. Wang T, Xu A, Zhang H. 1994 Evolution of vector magnetic fields and vertical currents and their relationship with solar flares in AR 5747. *Solar Phys.* **155**, 99–112. (doi:10.1007/BF00670733)
35. Leka KD, Canfield RC, McClymont AN, van Driel-Gesztelyi L. 1996 Evidence for current-carrying emerging flux. *Astrophys. J.* **462**, 547. (doi:10.1086/177171)
36. Sun X, Hoeksema JT, Liu Y, Wiegelmann T, Hayashi K, Chen Q, Thalmann J. 2012 Evolution of magnetic field and energy in a major eruptive active region based on SDO/HMI observation. *Astrophys. J.* **748**, 77. (doi:10.1088/0004-637X/748/2/77)
37. Tziotziou K, Georgoulis MK, Liu Y. 2013 Interpreting eruptive behavior in NOAA AR 11158 via the Region's magnetic energy and relative-helicity budgets. *Astrophys. J.* **772**, 115. (doi:10.1088/0004-637X/772/2/115)
38. Nindos A, Zhang H. 2002 Photospheric motions and coronal mass ejection productivity. *Astrophys. J. Lett.* **573**, L133–L136. (doi:10.1086/341937)
39. Nindos A, Patsourakos S, Wiegelmann T. 2012 On the role of the background overlying magnetic field in solar eruptions. *Astrophys. J. Lett.* **748**, L6. (doi:10.1088/2041-8205/748/1/L6)
40. van Ballegooijen AA, Martens PCH. 1989 Formation and eruption of solar prominences. *Astrophys. J.* **343**, 971–984. (doi:10.1086/167766)
41. van Driel-Gesztelyi L, Malherbe JM, Démoulin P. 2000 Emergence of a U-loop – sub-photospheric link between solar active regions. *Astron. Astrophys.* **364**, 845–852.
42. Yardley SL, Green LM, van Driel-Gesztelyi L, Williams DR, Mackay DH. 2018 The role of flux cancellation in eruptions from bipolar ARs. *Astrophys. J.* **866**, 8. (doi:10.3847/1538-4357/aade4a)
43. White SM. 2004 Coronal magnetic field measurements through gyroresonance emission. In *Astrophysics and space science library* (eds DE Gary, CU Keller). Astrophysics and space science library, no. 314. p. 89.
44. Ouyang Y, Zhou YH, Chen PF, Fang C. 2017 Chirality and magnetic configurations of solar filaments. *Astrophys. J.* **835**, 94. (doi:10.3847/1538-4357/835/1/94)
45. Schmieder B, Mein P, Mein N, Levens PJ, Labrosse N, Ofman L. 2017 Hα doppler shifts in a tornado in the solar corona. *Astron. Astrophys.* **597**, A109. (doi:10.1051/0004-6361/201628771)
46. Yan Y, Deng Y, Karlický M, Fu Q, Wang S, Liu Y. 2001 The magnetic rope structure and associated energetic processes in the 2000 July 14 solar flare. *Astrophys. J. Lett.* **551**, L115–L119. (doi:10.1086/319829)
47. Bleybel A, Amari T, van Driel-Gesztelyi L, Leka KD. 2002 Global budget for an eruptive active region. I. Equilibrium reconstruction approach. *Astron. Astrophys.* **395**, 685–695. (doi:10.1051/0004-6361:20021332)
48. Canou A, Amari T, Bommier V, Schmieder B, Aulanier G, Li H. 2009 Evidence for a pre-eruptive twisted flux rope using the themis vector magnetograph. *Astrophys. J. Lett.* **693**, L27–L30. (doi:10.1088/0004-637X/693/1/L27)
49. Guo Y, Schmieder B, Démoulin P, Wiegelmann T, Aulanier G, Török T, Bommier V. 2010 Coexisting flux rope and dipped arcade sections along one solar filament. *Astrophys. J.* **714**, 343–354. (doi:10.1088/0004-637X/714/1/343)

50. Guo Y, Ding MD, Schmieder B, Démoulin P, Li H. 2012 Evolution of hard X-ray sources and ultraviolet solar flare ribbons for a confined eruption of a magnetic flux rope. *Astrophys. J.* **746**, 17. (doi:10.1088/0004-637X/746/1/17)
51. Janvier M, Savcheva A, Pariat E, Tassev S, Millholland S, Bommier V, McCauley P, McKillop S, Dougan F. 2016 Evolution of flare ribbons, electric currents, and quasi-separatrix layers during an X-class flare. *Astron. Astrophys.* **591**, A141. (doi:10.1051/0004-6361/201628406)
52. Sun X, Hoeksema JT, Liu Y, Kazachenko M, Chen R. 2017 Investigating the magnetic imprints of major solar eruptions with SDO/HMI High-cadence vector magnetograms. *Astrophys. J.* **839**, 67. (doi:10.3847/1538-4357/aa69c1)
53. Guo Y *et al.* 2017 Magnetic helicity estimations in models and observations of the solar magnetic field. III. Twist number method. *Astrophys. J.* **840**, 40. (doi:10.3847/1538-4357/aa6aa8)
54. Canfield RC, Hudson HS, McKenzie DE. 1999 Sigmoidal morphology and eruptive solar activity. *Geophys. Res. Lett.* **26**, 627–630. (doi:10.1029/1999GL900105)
55. Rust DM, Kumar A. 1996 Evidence for helically kinked magnetic flux ropes in solar eruptions. *Astrophys. J. Lett.* **464**, L199. (doi:10.1086/310118)
56. Titov VS, Démoulin P. 1999 Basic topology of twisted magnetic configurations in solar flares. *Astron. Astrophys.* **351**, 707–720.
57. Green LM, Kliem B, Wallace AJ. 2011 Photospheric flux cancellation and associated flux rope formation and eruption. *Astron. Astrophys.* **526**, A2. (doi:10.1051/0004-6361/201015146)
58. Antiochos SK, Dahlburg RB, Klimchuk JA. 1994 The magnetic field of solar prominences. *Astrophys. J. Lett.* **420**, L41–L44. (doi:10.1086/187158)
59. Savcheva AS, McKillop SC, McCauley PI, Hanson EM, DeLuca EE. 2014 A new sigmoid catalog from hinode and the solar dynamics observatory: statistical properties and evolutionary histories. *Solar Phys.* **289**, 3297–3311. (doi:10.1007/s11207-013-0469-3)
60. Green LM, Kliem B. 2014 Observations of flux rope formation prior to coronal mass ejections. In *Nature of prominences and their role in space weather* (eds B Schmieder, JM Malherbe, ST Wu). IAU Symposium, no. 300, pp. 209–214.
61. Liu R, Liu C, Wang S, Deng N, Wang H. 2010 Sigmoid-to-flux-rope transition leading to a loop-like coronal mass ejection. *Astrophys. J. Lett.* **725**, L84–L90. (doi:10.1088/2041-8205/725/1/L84)
62. James AW, Green LM, Palmerio E, Valori G, Reid HAS, Baker D, Brooks DH, van Driel-Gesztelyi L, Kilpua EKJ. 2017 On-disc observations of flux rope formation prior to its eruption. *Solar Phys.* **292**, 71. (doi:10.1007/s11207-017-1093-4)
63. Nindos A, Patsourakos S, Vourlidas A, Tagikas C. 2015 How common are hot magnetic flux ropes in the low solar corona? A statistical study of EUV observations. *Astrophys. J.* **808**, 117. (doi:10.1088/0004-637X/808/2/117)
64. Patsourakos S, Vourlidas A, Stenborg G. 2013 Direct evidence for a fast coronal mass ejection driven by the prior formation and subsequent destabilization of a magnetic flux rope. *Astrophys. J.* **764**, 125. (doi:10.1088/0004-637X/764/2/125)
65. Zhang J, Cheng X, Ding MD. 2012 Observation of an evolving magnetic flux rope before and during a solar eruption. *Nature Commun.* **3**, 747. (doi:10.1038/ncomms1753)
66. Cheng X, Zhang J, Ding MD, Liu Y, Poomvises W. 2013 The driver of coronal mass ejections in the low corona: a flux rope. *Astrophys. J.* **763**, 43. (doi:10.1088/0004-637X/763/1/43)
67. Cheng X, Zhang J, Liu Y, Ding MD. 2011 Observing flux rope formation during the impulsive phase of a solar eruption. *Astrophys. J. Lett.* **732**, L25. (doi:10.1088/2041-8205/732/2/L25)
68. Song HQ, Zhang J, Chen Y, Cheng X. 2014 Direct observations of magnetic flux rope formation during a solar coronal mass ejection. *Astrophys. J. Lett.* **792**, L40. (doi:10.1088/2041-8205/792/2/L40)
69. Zhang J, Dere KP, Howard RA, Kundu MR, White SM. 2001 On the temporal relationship between coronal mass ejections and flares. *Astrophys. J.* **559**, 452–462. (doi:10.1086/322405)
70. Zhang J, Dere KP. 2006 A statistical study of main and residual accelerations of coronal mass ejections. *Astrophys. J.* **649**, 1100–1109. (doi:10.1086/506903)
71. Carmichael H. 1964 A process for flares. *NASA Special Publ.* **50**, 451.
72. Sturrock PA. 1966 Model of the high-energy phase of solar flares. *Nature* **211**, 695–697. (doi:10.1038/211695a0)

73. Hirayama T. 1974 Theoretical model of flares and prominences. I: evaporating flare model. *Solar Phys.* **34**, 323–338. (doi:10.1007/BF00153671)
74. Koppa RA, Pneuman GW. 1976 Magnetic reconnection in the corona and the loop prominence phenomenon. *Solar Phys.* **50**, 85–98. (doi:10.1007/BF00206193)
75. McKenzie DE. 2002 Signatures of reconnection in eruptive flares [Invited]. In *Multi-wavelength observations of coronal structure and dynamics* (eds PCH Martens, D Cauffman), p. 155. London, UK: Pergamon.
76. Shibata K, Masuda S, Shimojo M, Hara H, Yokoyama T, Tsuneta S, Kosugi T, Ogawara Y. 1995 Hot-plasma ejections associated with compact-loop solar flares. *Astrophys. J. Lett.* **451**, L83. (doi:10.1086/309688)
77. Aulanier G, Janvier M, Schmieder B. 2012 The standard flare model in three dimensions. I. Strong-to-weak shear transition in post-flare loops. *Astron. Astrophys.* **543**, A110. (doi:10.1051/0004-6361/201219311)
78. Aulanier G, Démoulin P, Schrijver CJ, Janvier M, Pariat E, Schmieder B. 2013 The standard flare model in three dimensions. II. Upper limit on solar flare energy. *Astron. Astrophys.* **549**, A66. (doi:10.1051/0004-6361/201220406)
79. Janvier M, Aulanier G, Pariat E, Demoulin P. 2013 The standard flare model in three dimensions. III. Slip-running reconnection properties. *Astron. Astrophys.* **555**, A77. (doi:10.1051/0004-6361/201321164)
80. Aulanier G, Dudík J. 2019 Drifting of the line-tied footpoints of CME flux-ropes. *Astron. Astrophys.* **621**, A72. (doi:10.1051/0004-6361/201834221)
81. Harrison RA. 1995 The nature of solar flares associated with coronal mass ejection. *Astron. Astrophys.* **304**, 585.
82. Temmer M, Veronig AM, Kontar EP, Krucker S, Vršnak B. 2010 Combined STEREO/RHESSI study of coronal mass ejection acceleration and particle acceleration in solar flares. *Astrophys. J.* **712**, 1410–1420. (doi:10.1088/0004-637X/712/2/1410)
83. Moore RL, Sterling AC, Hudson HS, Lemen JR. 2001 Onset of the magnetic explosion in solar flares and coronal mass ejections. *Astrophys. J.* **552**, 833–848. (doi:10.1086/320559)
84. Török T, Kliem B. 2005 Confined and ejective eruptions of kink-unstable flux ropes. *Astrophys. J. Lett.* **630**, L97–L100. (doi:10.1086/462412)
85. Parker EN. 1996 Comment on 'Current paths in the corona and energy release in solar flares'. *Astrophys. J.* **471**, 489. (doi:10.1086/177984)
86. Chandrasekhar S. 1956 On force-free magnetic fields. *Proc. Natl Acad. Sci. USA* **42**, 1–5. (doi:10.1073/pnas.42.1.1)
87. Chandrasekhar S. 1961 *Hydrodynamic and hydromagnetic stability*. New York, NY: Dover Publications.
88. Sakurai T. 1981 Calculation of force-free magnetic field with non-constant α. *Solar Phys.* **69**, 343–359. (doi:10.1007/BF00149999)
89. Alissandrakis CE. 1981 On the computation of constant alpha force-free magnetic field. *Astron. Astrophys.* **100**, 197–200.
90. Rosner R, Vaiana GS. 1978 Cosmic flare transients - constraints upon models for energy storage and release derived from the event frequency distribution. *Astrophys. J.* **222**, 1104–1108. (doi:10.1086/156227)
91. Woltjer L. 1958 A theorem on force-free magnetic fields. *Proc. Natl Acad. Sci. USA* **44**, 489–491. (doi:10.1073/pnas.44.6.489)
92. Berger MA, Field GB. 1984 The topological properties of magnetic helicity. *J. Fluid Mech.* **147**, 133–148. (doi:10.1017/S0022112084002019)
93. Berger MA. 1999 Introduction to magnetic helicity. *Plasma Phys. Control. Fusion* **41**, B167–B175. (doi:10.1088/0741-3335/41/12B/312)
94. Pariat E, Valori G, Démoulin P, Dalmasse K. 2015 Testing magnetic helicity conservation in a solar-like active event. *Astron. Astrophys.* **580**, A128. (doi:10.1051/0004-6361/201525811)
95. Taylor JB. 1974 Relaxation of toroidal plasma and generation of reverse magnetic fields. *Phys. Rev. Lett.* **33**, 1139–1141. (doi:10.1103/PhysRevLett.33.1139)
96. Taylor JB. 1986 Relaxation and magnetic reconnection in plasmas. *Rev. Mod. Phys.* **58**, 741–763. (doi:10.1103/RevModPhys.58.741)

97. Georgoulis MK, LaBonte BJ. 2007 Magnetic energy and helicity budgets in the active region solar corona. I. Linear force-free approximation. *Astrophys. J.* **671**, 1034–1050. (doi:10.1086/521417)
98. Kusano K, Suzuki Y, Kubo H, Miyoshi T, Nishikawa K. 1994 Three-dimensional simulation study of the magnetohydrodynamic relaxation process in the solar corona. 1: spontaneous generation of Taylor-Heyvaerts-Priest state. *Astrophys. J.* **433**, 361–378. (doi:10.1086/174651)
99. Antiochos SK, DeVore CR. 1999 The role of helicity in magnetic reconnection: 3D numerical simulations. In *Geophysical Monograph Series* (eds MR Brown RC Canfield, AA Pevtsov), vol. 111, p. 187. Washington, DC.
100. Dalmasse K, Chandra R, Schmieder B, Aulanier G. 2015 Can we explain atypical solar flares? *Astron. Astrophys.* **574**, A37. (doi:10.1051/0004-6361/201323206)
101. Low BC. 1994 Magnetohydrodynamic processes in the solar corona: flares, coronal mass ejections, and magnetic helicity. *Phys. Plasmas* **1**, 1684–1690. (doi:10.1063/1.870671)
102. Pevtsov AA, Canfield RC, Metcalf TR. 1995 Latitudinal variation of helicity of photospheric magnetic fields. *Astrophys. J. Lett.* **440**, L109–L112. (doi:10.1086/187773)
103. Rust DM. 2003 The helicial flux rope structure of solar filaments. *Adv. Space Res.* **32**, 1895–1903. (doi:10.1016/S0273-1177(03)90623-5)
104. Rust DM, LaBonte BJ. 2005 Observational evidence of the kink instability in solar filament eruptions and sigmoids. *Astrophys. J. Lett.* **622**, L69–L72. (doi:10.1086/429379)
105. Kusano K, Maeshiro T, Yokoyama T, Sakurai T. 2004 The trigger mechanism of solar flares in a coronal arcade with reversed magnetic shear. *Astrophys. J.* **610**, 537–549. (doi:10.1086/421547)
106. Pevtsov AA, Berger MA, Nindos A, Norton AA, van Driel-Gesztelyi L. 2014 Magnetic helicity, tilt, and twist. *Space Sci. Rev.* **186**, 285–324. (doi:10.1007/s11214-014-0082-2)
107. Georgoulis MK, Rust DM, Pevtsov AA, Bernasconi PN, Kuzanyan KM. 2009 Solar magnetic helicity injected into the heliosphere: magnitude, balance, and periodicities over solar cycle 23. *Astrophys. J. Lett.* **705**, L48–L52. (doi:10.1088/0004-637X/705/1/L48)
108. Villadsen JR. 2017 The search for stellar coronal mass ejections. PhD thesis, California Institute of Technology, Pasadena, CA.
109. Seehafer N. 1990 Electric current helicity in the solar atmosphere. *Solar Phys.* **125**, 219–232. (doi:10.1007/BF00158402)
110. Bao S, Zhang H. 1998 Patterns of current helicity for the twenty-second solar cycle. *Astrophys. J. Lett.* **496**, L43–L46. (doi:10.1086/311232)
111. Komm R, Howe R, Hill F, González Hernández I, Toner C. 2005 Kinetic helicity density in solar subsurface layers and flare activity of active regions. *Astrophys. J.* **630**, 1184–1193. (doi:10.1086/432031)
112. Reinard AA, Henthorn J, Komm R, Hill F. 2010 Evidence that temporal changes in solar subsurface helicity precede active region flaring. *Astrophys. J. Lett.* **710**, L121–L125. (doi:10.1088/2041-8205/710/2/L121)
113. Gao Y, Zhao J, Zhang H. 2012 Analysis on correlations between subsurface kinetic helicity and photospheric current helicity in active regions. *Astrophys. J. Lett.* **761**, L9. (doi:10.1088/2041-8205/761/1/L9)
114. Gao Y, Zhao J, Zhang H. 2014 A study of connections between solar flares and subsurface flow fields of active regions. *Solar Phys.* **289**, 493–502. (doi:10.1007/s11207-013-0274-z)
115. Kusano K, Maeshiro T, Yokoyama T, Sakurai T. 2002 Measurement of magnetic helicity injection and free energy loading into the solar corona. *Astrophys. J.* **577**, 501–512. (doi:10.1086/342171)
116. Nindos A, Zhang J, Zhang H. 2003 The magnetic helicity budget of solar active regions and coronal mass ejections. *Astrophys. J.* **594**, 1033–1048. (doi:10.1086/377126)
117. Démoulin P, Berger MA. 2003 Magnetic energy and helicity fluxes at the photospheric level. *Solar Phys.* **215**, 203–215. (doi:10.1023/A:1025679813955)
118. Welsch BT, Abbett WP, De Rosa ML, Fisher GH, Georgoulis MK, Kusano K, Longcope DW, Ravindra B, Schuck PW. 2007 Tests and comparisons of velocity-inversion techniques. *Astrophys. J.* **670**, 1434–1452. (doi:10.1086/522422)
119. Chae J. 2001 Observational determination of the rate of magnetic helicity transport through the solar surface via the horizontal motion of field line footpoints. *Astrophys. J. Lett.* **560**, L95–L98. (doi:10.1086/324173)

120. Zhang H, Brandenburg A, Sokoloff DD. 2014 Magnetic helicity and energy spectra of a solar active region. *Astrophys. J. Lett.* **784**, L45. (doi:10.1088/2041-8205/784/2/L45)
121. Zhang H, Brandenburg A, Sokoloff DD. 2016 Evolution of magnetic helicity and energy spectra of solar active regions. *Astrophys. J.* **819**, 146. (doi:10.3847/0004-637X/819/2/146)
122. Zhang H, Brandenburg A. 2018 Solar kinetic energy and cross helicity spectra. *Astrophys. J. Lett.* **862**, L17. (doi:10.3847/2041-8213/aad337)
123. Moffatt HK. 1969 The degree of knottedness of tangled vortex lines. *J. Fluid Mech.* **35**, 117–129. (doi:10.1017/S0022112069000991)
124. Yeates AR, Hornig G. 2016 The global distribution of magnetic helicity in the solar corona. *Astron. Astrophys.* **594**, A98. (doi:10.1051/0004-6361/201629122)
125. Guo Y *et al.* 2017 Magnetic helicity estimations in models and observations of the solar magnetic field. III. Twist number method. *Astrophys. J.* **840**, 40. (doi:10.3847/1538-4357/aa6aa8)
126. Valori G *et al.* 2016 Magnetic helicity estimations in models and observations of the solar magnetic field. Part I: finite volume methods. *Space Sci. Rev.* **201**, 147–200. (doi:10.1007/s11214-016-0299-3)
127. Georgoulis MK, Tziotziou K, Raouafi NE. 2012 Magnetic energy and helicity budgets in the active-region solar corona. II. Nonlinear force-free approximation. *Astrophys. J.* **759**, 1. (doi:10.1088/0004-637X/759/1/1)
128. Démoulin P, Pariat E, Berger MA. 2006 Basic properties of mutual magnetic helicity. *Solar Phys.* **233**, 3–27. (doi:10.1007/s11207-006-0010-z)
129. Nindos A, Andrews MD. 2004 The association of big flares and coronal mass ejections: what is the role of magnetic helicity? *Astrophys. J. Lett.* **616**, L175–L178. (doi:10.1086/426861)
130. LaBonte BJ, Georgoulis MK, Rust DM. 2007 Survey of magnetic helicity injection in regions producing X-class flares. *Astrophys. J.* **671**, 955–963. (doi:10.1086/522682)
131. Bao SD, Zhang HQ, Ai GX, Zhang M. 1999 A survey of flares and current helicity in active regions. *Astron. Astrophys. Suppl.* **139**, 311–320. (doi:10.1051/aas:1999396)
132. Yang X, Zhang H, Gao Y, Guo J, Lin G. 2012 A statistical study on photospheric magnetic nonpotentiality of active regions and its relationship with flares during solar cycles 22–23. *Solar Phys.* **280**, 165–181. (doi:10.1007/s11207-012-0061-2)
133. Tziotziou K, Georgoulis MK, Raouafi NE. 2012 The magnetic energy-helicity diagram of solar active regions. *Astrophys. J. Lett.* **759**, L4. (doi:10.1088/2041-8205/759/1/L4)
134. Tziotziou K, Moraitis K, Georgoulis MK, Archontis V. 2014 Validation of the magnetic energy vs. helicity scaling in solar magnetic structures. *Astron. Astrophys.* **570**, L1. (doi:10.1051/0004-6361/201424864)
135. Tziotziou K, Park SH, Tsiropoula G, Kontogiannis I. 2015 Energy and helicity injection in solar quiet regions. *Astron. Astrophys.* **581**, A61. (doi:10.1051/0004-6361/201526389)
136. Patsourakos S *et al.* 2016 The major geoeffective solar eruptions of 2012 March 7: comprehensive sun-to-earth analysis. *Astrophys. J.* **817**, 14. (doi:10.3847/0004-637X/817/1/14)
137. Georgoulis MK, Titov VS, Mikić Z. 2012 Non-neutralized electric current patterns in solar active regions: origin of the shear-generating lorentz force. *Astrophys. J.* **761**, 61. (doi:10.1088/0004-637X/761/1/61)
138. Melrose DB. 1995 Current paths in the corona and energy release in solar flares. *Astrophys. J.* **451**, 391. (doi:10.1086/176228)
139. DeVore CR. 2000 Magnetic helicity generation by solar differential rotation. *Astrophys. J.* **539**, 944–953. (doi:10.1086/309274)
140. Zhang M, Flyer N. 2008 The dependence of the helicity bound of force-free magnetic fields on boundary conditions. *Astrophys. J.* **683**, 1160–1167. (doi:10.1086/589993)
141. Su Y *et al.* 2007 Evolution of the sheared magnetic fields of two X-class flares observed by hinode/XRT. *Publ. Astron. Soc. Jpn.* **59**, S785–S791. (doi:10.1093/pasj/59.sp3.S785)
142. Thalmann JK, Su Y, Temmer M, Veronig AM. 2015 The confined X-class flares of solar active region 2192. *Astrophys. J. Lett.* **801**, L23. (doi:10.1088/2041-8205/801/2/L23)
143. Green LM, López fuentes MC, Mandrini CH, Démoulin P, Van Driel-Gesztelyi L, CulhaneJL JL. 2002 The magnetic helicity budget of a CME-prolific active region. *Solar Phys.* **208**, 43–68. (doi:10.1023/A:1019658520033)

144. Manchester W, Low BC. 2000 Magnetostatic atmospheres possessing identical invariants of ideal magnetohydrodynamics. *Phys. Plasmas* **7**, 1263–1279. (doi:10.1063/1.873937)
145. Manchester IV W. 2001 The role of nonlinear Alfvén waves in shear formation during solar magnetic flux emergence. *Astrophys. J.* **547**, 503–519. (doi:10.1086/318342)
146. Manchester IV W, Gombosi T, DeZeeuw D, Fan Y. 2004 Eruption of a buoyantly emerging magnetic flux rope. *Astrophys. J.* **610**, 588–596. (doi:10.1086/421516)
147. Manchester IV W. 2007 Solar atmospheric dynamic coupling due to shear motions driven by the lorentz force. *Astrophys. J.* **666**, 532–540. (doi:10.1086/520493)
148. Török T, Leake JE, Titov VS, Archontis V, Mikić Z, Linton MG, Dalmasse K, Aulanier G, Kliem B. 2014 Distribution of electric currents in solar active regions. *Astrophys. J. Lett.* **782**, L10. (doi:10.1088/2041-8205/782/1/L10)
149. López Fuentes MC, Démoulin P, Mandrini CH, Pevtsov AA, van Driel-Gesztelyi L. 2003 Magnetic twist and writhe of active regions. On the origin of deformed flux tubes. *Astron. Astrophys.* **397**, 305–318. (doi:10.1051/0004-6361:20021487)
150. Georgoulis MK, LaBonte BJ. 2004 Vertical lorentz force and cross-field currents in the photospheric magnetic fields of solar active regions. *Astrophys. J.* **615**, 1029–1041. (doi:10.1086/424501)
151. Fisher GH, Bercik DJ, Welsch BT, Hudson HS. 2012 Global forces in eruptive solar flares: the lorentz force acting on the solar atmosphere and the solar interior. *Solar Phys.* **277**, 59–76. (doi:10.1007/s11207-011-9907-2)
152. Forbes TG. 2000 A review on the genesis of coronal mass ejections. *J. Geophys. Res. (Space)* **105**, 23153–23166. (doi:10.1029/2000JA000005)
153. Aulanier G. 2014 The physical mechanisms that initiate and drive solar eruptions. In *Nature of prominences and their role in space weather* (eds B Schmieder, JM Malherbe, ST Wu). IAU Symposium, no. 300, pp. 184–196.
154. Mikic Z, Linker JS. 1994 Disruption of coronal magnetic field arcades. *Astrophys. J.* **430**, 898–912. (doi:10.1086/174460)
155. Wolfson R. 1995 Shear-induced opening of the coronal magnetic field. *Astrophys. J.* **443**, 810–817. (doi:10.1086/175571)
156. van der Holst B, Manchester IV W, Sokolov IV, Tóth G, Gombosi TI, DeZeeuw D, Cohen O. 2009 Breakout coronal mass ejection or streamer blowout: the bugle effect. *Astrophys. J.* **693**, 1178–1187. (doi:10.1088/0004-637X/693/2/1178)
157. Amari T, Luciani JF, Aly JJ, Tagger M. 1996 Very fast opening of a three-dimensional twisted magnetic flux tube. *Astrophys. J. Lett.* **466**, L39. (doi:10.1086/310158)
158. Török T, Kliem B. 2003 The evolution of twisting coronal magnetic flux tubes. *Astron. Astrophys.* **406**, 1043–1059. (doi:10.1051/0004-6361:20030692)
159. Aulanier G, Démoulin P, Grappin R. 2005 Equilibrium and observational properties of line-tied twisted flux tubes. *Astron. Astrophys.* **430**, 1067–1087. (doi:10.1051/0004-6361:20041519)
160. Amari T, Luciani JF, Aly JJ, Mikic Z, Linker J. 2003 Coronal mass ejection: initiation, magnetic helicity, and flux ropes. I. Boundary motion-driven evolution. *Astrophys. J.* **585**, 1073–1086. (doi:10.1086/345501)
161. Roussev II, Sokolov IV, Forbes TG, Gombosi TI, Lee MA, Sakai JI. 2004 A numerical model of a coronal mass ejection: shock development with implications for the acceleration of gev protons. *Astrophys. J. Lett.* **605**, L73–L76. (doi:10.1086/392504)
162. Mikić Z, Lionello R, Mok Y, Linker JA, Winebarger AR. 2013 The importance of geometric effects in coronal loop models. *Astrophys. J.* **773**, 94. (doi:10.1088/0004-637X/773/2/94)
163. Fan Y. 2001 The emergence of a twisted Ω-tube into the solar atmosphere. *Astrophys. J. Lett.* **554**, L111–L114. (doi:10.1086/320935)
164. Magara T. 2004 A model for dynamic evolution of emerging magnetic fields in the sun. *Astrophys. J.* **605**, 480–492. (doi:10.1086/382148)
165. Archontis V, Hood AW. 2008 A flux emergence model for solar eruptions. *Astrophys. J. Lett.* **674**, L113. (doi:10.1086/529377)
166. Archontis V, Hood AW. 2012 Magnetic flux emergence: a precursor of solar plasma expulsion. *Astron. Astrophys.* **537**, A62. (doi:10.1051/0004-6361/201116956)
167. Leake JE, Linton MG, Török T. 2013 Simulations of emerging magnetic flux. I. The formation of stable coronal flux ropes. *Astrophys. J.* **778**, 99. (doi:10.1088/0004-637X/778/2/99)

168. Leake JE, Linton MG, Antiochos SK. 2014 Simulations of emerging magnetic flux. II. The formation of unstable coronal flux ropes and the initiation of coronal mass ejections. *Astrophys. J.* **787**, 46. (doi:10.1088/0004-637X/787/1/46)
169. Forbes TG, Isenberg PA. 1991 A catastrophe mechanism for coronal mass ejections. *Astrophys. J.* **373**, 294–307. (doi:10.1086/170051)
170. Isenberg PA, Forbes TG, Demoulin P. 1993 Catastrophic evolution of a force-free flux rope: a model for eruptive flares. *Astrophys. J.* **417**, 368. (doi:10.1086/173319)
171. Lin J, Forbes TG, Isenberg PA. 2001 Prominence eruptions and coronal mass ejections triggered by newly emerging flux. *J. Geophys. Res. (Space)* **106**, 25 053–25 074. (doi:10.1029/2001JA000046)
172. Lin J, van Ballegooijen AA. 2002 Catastrophic and noncatastrophic mechanisms for coronal mass ejections. *Astrophys. J.* **576**, 485–492. (doi:10.1086/341737)
173. Priest E. 2014 *Magnetohydrodynamics of the sun*. Cambridge, UK: Cambridge University Press.
174. Démoulin P, Aulanier G. 2010 Criteria for flux rope eruption: non-equilibrium versus torus instability. *Astrophys. J.* **718**, 1388–1399. (doi:10.1088/0004-637X/718/2/1388)
175. Kliem B, Török T. 2006 Torus instability. *Phys. Rev. Lett.* **96**, 255002. (doi:10.1103/PhysRevLett.96.255002)
176. Olmedo O, Zhang J. 2010 Partial torus instability. *Astrophys. J.* **718**, 433–440. (doi:10.1088/0004-637X/718/1/433)
177. Török T, Kliem B. 2007 Numerical simulations of fast and slow coronal mass ejections. *Astron. Nachr.* **328**, 743. (doi:10.1002/asna.200710795)
178. Török T, Kliem B. 2004 The kink instability of a coronal magnetic loop as a trigger mechanism for solar eruptions. *Pub. of Astron. Dept. Eotvos Lorand U.* **14**, 165–176.
179. Jacobs C, Poedts S, van der Holst B. 2006 The effect of the solar wind on CME triggering by magnetic foot point shearing. *Astron. Astrophys.* **450**, 793–803. (doi:10.1051/0004-6361:20054670)
180. Antiochos SK, DeVore CR, Klimchuk JA. 1999 A model for solar coronal mass ejections. *Astrophys. J.* **510**, 485–493. (doi:10.1086/306563)
181. MacNeice P, Antiochos SK, Phillips A, Spicer DS, DeVore CR, Olson K. 2004 A numerical study of the breakout model for coronal mass ejection initiation. *Astrophys. J.* **614**, 1028–1041. (doi:10.1086/423887)
182. Karpen JT, Antiochos SK, DeVore CR. 2012 The mechanisms for the onset and explosive eruption of coronal mass ejections and eruptive flares. *Astrophys. J.* **760**, 81. (doi:10.1088/0004-637X/760/1/81)
183. Lynch BJ, Edmondson JK. 2013 Sympathetic magnetic breakout coronal mass ejections from pseudostreamers. *Astrophys. J.* **764**, 87. (doi:10.1088/0004-637X/764/1/87)
184. Lynch BJ, Antiochos SK, DeVore CR, Luhmann JG, Zurbuchen TH. 2008 Topological evolution of a fast magnetic breakout CME ilions. *Astrophys. J.* **683**, 1192–1206. (doi:10.1086/589738)
185. Aulanier G, DeLuca EE, Antiochos SK, McMullen RA, Golub L. 2000 The topology and evolution of the bastille day flare. *Astrophys. J.* **540**, 1126–1142. (doi:10.1086/309376)
186. Ugarte Urra I, Warren HP, Winebarger AR. 2007 The magnetic topology of coronal mass ejection sources. *Astrophys. J.* **662**, 1293–1301. (doi:10.1086/514814)
187. Sterling AC, Moore RL. 2004 Evidence for gradual external reconnection before explosive eruption of a solar filament. *Astrophys. J.* **602**, 1024–1036. (doi:10.1086/379763)
188. Chen J. 1989 Effects of toroidal forces in current loops embedded in a background plasma. *Astrophys. J.* **338**, 453–470. (doi:10.1086/167211)
189. Chen J. 1996 Theory of prominence eruption and propagation: interplanetary consequences. *J. Geophys. Res. (Space)* **101**, 27499–27520. (doi:10.1029/96JA02644)
190. Krall J, Chen J, Santoro R. 2000 Drive mechanisms of erupting solar magnetic flux ropes. *Astrophys. J.* **539**, 964–982. (doi:10.1086/309256)
191. Chen J, Kunkel V. 2010 Temporal and physical connection between coronal mass ejections and flares. *Astrophys. J.* **717**, 1105–1122. (doi:10.1088/0004-637X/717/2/1105)
192. Chen J. 2017 Physics of erupting solar flux ropes: coronal mass ejections (CMEs)—recent advances in theory and observation. *Phys. Plasmas* **24**, 090501. (doi:10.1063/1.4993929)

193. Kunkel V, Chen J. 2010 Evolution of a coronal mass ejection and its magnetic field in interplanetary space. *Astrophys. J. Lett.* **715**, L80–L83. (doi:10.1088/2041-8205/715/2/L80)
194. Schuck PW. 2010 The photospheric energy and helicity budgets of the flux-injection hypothesis. *Astrophys. J.* **714**, 68–88. (doi:10.1088/0004-637X/714/1/68)
195. Aschwanden MJ *et al.* 2016 25 Years of self-organized criticality: solar and astrophysics. *Space Sci. Rev.* **198**, 47–166. (doi:10.1007/s11214-014-0054-6)
196. Parker EN. 1988 Nanoflares and the solar X-ray corona. *Astrophys. J.* **330**, 474–479. (doi:10.1086/166485)
197. Sun X *et al.* 2015 Why is the great solar active region 12192 flare-rich but CME-poor? *Astrophys. J. Lett.* **804**, L28. (doi:10.1088/2041-8205/804/2/L28)
198. Sarkar R, Srivastava N. 2018 A comparative study of the eruptive and non-eruptive flares produced by the largest active region of solar cycle 24. *Solar Phys.* **293**, 16. (doi:10.1007/s11207-017-1235-8)
199. Socas-Navarro H. 2005 The three-dimensional structure of a sunspot magnetic field. *Astrophys. J. Lett.* **631**, L167–L170. (doi:10.1086/497334)
200. Borrero JM, Ichimoto K. 2011 Magnetic structure of sunspots. *Living Rev. Solar Phys.* **8**, 4. (doi:10.12942/lrsp-2011-4)